THE RESPONSE OF CYLINDRICAL SHELLS TO RANDOM ACOUSTIC EXCITATION OVER BROAD FREQUENCY RANGES

by
Daniel D. Kana
Wen-Hwa Chu
Roger L. Bessey

FINAL REPORT
Contract No. NAS8-21479
Control No. DCN 1-9-53-20039 (1F)
SwRI Project No. 02-2396

Prepared for

National Aeronautics and Space Administration
George C. Marshall Space Flight Center
Marshall Space Flight Center, Alabama

September 1, 1970

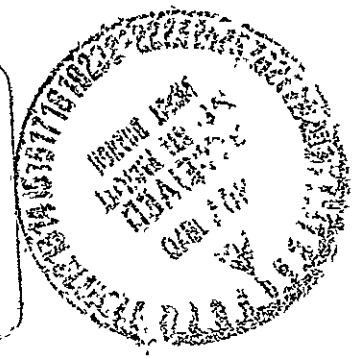

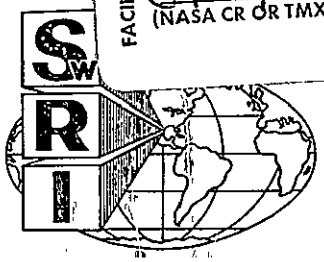

SOUTHWEST RESEARCH INSTITUTE
SAN ANTONIO HOUSTON

NASA CR-70-500.

THE RESPONSE OF CYLINDRICAL SHELLS TO RANDOM ACOUSTIC EXCITATION OVER BROAD FREQUENCY RANGES

by

Daniel D. Kana

Wen-Hwa Chu

Roger L. Bessey

FINAL REPORT

Contract No. NAS8-21479

Control No. DCN 1-9-53-20039 (1F)

SwRI Project No. 02-2396

Prepared for

National Aeronautics and Space Administration

George C. Marshall Space Flight Center

Marshall Space Flight Center, Alabama

September 1, 1970

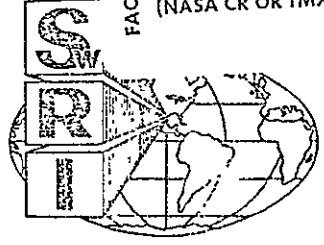

SOUTHWEST RESEARCH INSTITUTE

SAN ANTONIO HOUSTON

SOUTHWEST RESEARCH INSTITUTE
Post Office Drawer 28510, 8500 Culebra Road
San Antonio, Texas 78228

THE RESPONSE OF CYLINDRICAL SHELLS TO RANDOM ACOUSTIC EXCITATION OVER BROAD FREQUENCY RANGES

by
Daniel D. Kana
Wen-Hwa Chu
Roger L. Bessey

FINAL REPORT
Contract No. NAS8-21479
Control No. DCN 1-9-53-20039 (1F)
SwRI Project No. 02-2396

Prepared for

National Aeronautics and Space Administration
George C. Marshall Space Flight Center
Marshall Space Flight Center, Alabama

September 1, 1970

Approved:

H. Norman Abramson, Director
Department of Mechanical Sciences

ABSTRACT

The response of a closed cylindrical shell is determined for acoustic excitation which is random in time but deterministic in space. Two slightly different formulations of the statistical energy method are utilized to compute shell displacement and interior pressure responses which are compared with measured values in 1/3-octave frequency bands. Structural damping estimates are based on linear viscoelastic theory. Various 1/3-octave band averages are defined for computing other frequency-dependent parameters for the system. Rather good overall agreement between theoretical and experimental results for shell response is achieved when the non-ideal characteristics of the 1/3-octave filters are accounted for. On the other hand, agreement for interior pressure response was somewhat less satisfactory. A detailed discussion is given for several possible sources of discrepancy.

TABLE OF CONTENTS

	Page
LIST OF ILLUSTRATIONS	v
LIST OF TABLES	vi
LIST OF SYMBOLS	vii
INTRODUCTION	1
EXPERIMENTAL ANALYSIS	3
Description of Physical System	3
Calibration Procedures	12
Experiments Performed	18
THEORETICAL ANALYSIS	20
General Modal Relationships	20
Power Balance Equations	24
General Concepts	24
Detailed Derivation	25
Input Power	31
Coupling Factors	40
Loss Factors	44
Viscoelastic Structural Damping	44
Air Damping	50
RESULTS AND DISCUSSION	53
Comparison of Theory and Experiment	53
Supporting Results	62
RECOMMENDATIONS FOR FURTHER RESEARCH	75
ACKNOWLEDGMENTS	77
REFERENCES	78

TABLE OF CONTENTS (Cont'd)

		Page
APPENDICES		
A.	Spatial Distribution Parameters for Acoustical Field	80
B.	Speaker Calibration Factors	82
C.	Derivation of Eq. (49)	84
D.	Derivation of Eqs. (114b) and (105)	87

LIST OF ILLUSTRATIONS

Figure		Page
1	Coordinate System	4
2	Photograph of Apparatus	5
3	Schematic of Instrumentation	6
4	Spatial Distribution of Acoustic Field	15
5	Power Spectrum for Broad-Band Excitation	17
6	Modal Diagram for Cylindrical Shell	21
7	Modal Density of Cylindrical Shell	23
8	Damping Decrement for Cylindrical Shell	49
9	Energy Distribution for System	54
10	Shell Response Ratio	55
11	Air Cavity Response Ratio	56
12	Highly Resolved Shell Response	63
13	Highly Resolved Air Cavity Response	64
14	Top Plate Response Ratio	68

LIST OF TABLES

Table		Page
I	Properties of Test Cylinder	7
II	1/3-Octave Filter Center Frequencies and 1/2-Power Point Frequencies	10
III	Transducer Locations	11
IV	Equation Reference for Calculations	58
V	Energy Density Distribution	60

LIST OF SYMBOLS

A, A'	total area of cylindrical shell and area of applied excitation pressure, respectively; in^2
$A_0, B_0, P_0, E_0, D_0, G_0$	spatial distribution constants dependent on center frequency, ω (non-dimensional)
a	radius of tank; in.
$(a, 0, x_0)$	point of reference in (r, θ, x) coordinates on shell
B_{rm}	gyroscopic coupling coefficient between the scaled m^{th} shell modal equation and r^{th} air modal equation; rad/sec
c_ℓ	longitudinal wave velocity in shell medium; $\left\{E/[\rho_s(1 - \nu_e^2)]\right\}^{1/2}$ in./sec
c_0	sound velocity in the air medium; in./sec
E_3	total energy of the interior air with center frequency ω per unit bandwidth; (in.-lb)/(rad/sec)
$E_{2AF}, E_{2AS}, E_{2NR}, E_2$	AF, AS, NR and total energy of the shell per unit bandwidth with center frequency ω; (in.-lb)/(rad/sec)
E_a, E_s	energy per unit bandwidth of air and shell, respectively; (in.-lb)/(rad/sec)
F_m	scaled generalized force per unit mass of the m^{th} shell mode; in/sec^2
f, ω	frequency and circular frequency; Hz and rad/sec, respectively
f_1, f_2	force per unit mass applied to first and second oscillators, respectively; $in./sec^2$
f_r, f_c	shell ring frequency and coincidence frequency, respectively; Hz
$\hat{G}_{p'p''}, \hat{C}_{p'p''}$	cross-spectral and co-spectral density of excitation pressure, for pressure at x' and x'', respectively; $(psi)^2/(rad/sec)$

LIST OF SYMBOLS (Cont'd)

g_3	damping constant, same as loss factor η_3 (non-dimensional)
g_{mr}, g_{rm}	coupling coefficient between m^{th} shell mode and r^{th} air mode; rad/sec
I_s	number of s-type shell modes
$I_{2AF}, I_{2AS}, I_{2NR}, I_2$	number of modes for AF, AS, NR modes and the total number of modes of the shell in $(\omega, \Delta\omega)$
$I^2_{m_b}, J^2_{m_b}$	m^{th} joint acceptance integrals in $(\omega_b, \Delta\omega_b)$; in^2
I^2_{mn}, J^2_{mn}	mn^{th} joint acceptance integrals in $(\omega, \Delta\omega)$; in^2
i	$\sqrt{-1}$
$J_0(z), J_1(z)$	Bessel function of the first kind of order zero and unity
$\langle J^2_n \rangle_s$	average s-type joint acceptance per mode
$k_R(x,\omega), k_I(x,\omega)$	co and quad pressure cross-correlation factor (non-dimensional)
k_x, k_y, k_z, k_a	axial, circumferential and normal (radial) wave number of air modes in an equivalent rectangular room and the resultant wave number, respectively
M	total mass of the cylinder; $(lb\text{-}sec^2)/in.$
M_m	generalized mass of the m^{th} shell mode; $(lb\text{-}sec^2)/in.$
m, n	axial and circumferential wave number of shell modes (non-dimensional)
$N_s(\omega), N_r(\omega)$	total number of the s-type shell modes and the interior air medium, respectively (non-dimensional), in $(\omega, \Delta\omega)$
n_3, n_r	number of modes per unit bandwidth for the interior air; $(rad/sec)^{-1}$
$n_{2AF}, n_{2AS}, n_{2NR}, n_2$	number of modes per unit bandwidth for AF, AS, NR modes and the total number of the shell, respectively; $(rad/sec)^{-1}$

LIST OF SYMBOLS (Cont'd)

$P_{2_s}^{IN}, P_2^{IN}$	input power to the s-type shell modes and to the shell, respectively, per unit bandwidth with center frequency ω; (in-lb/sec)/(rad/sec)
p	pressure; psi
R	distance on projected area of applied pressure Eq. (51c); in.
R_{rad}	radiation resistance; $(lb\text{-}sec^2)/in./(rad/sec)$
r, θ, x	cylindrical coordinates
$S_{p0}(\omega)$	point reference pressure spectral density; $(psi)^2/(rad/sec)$
$S_w(x,\omega), S_{w_{av}}(\omega)$	spectral density of local and average top-plate displacement; $in^2/(rad/sec)$
$S_y(\omega), S_{p_3}(\omega)$	spectral density of the shell response and interior pressure $(in^2)/(rad/sec)$ and $(psi)^2/(rad/sec)$, respectively
S_m', q_r'	amplitude of the m^{th} and r^{th} shell and air mode, respectively; in.
s, q	scaled displacement of the shell and the air, respectively; in., unless otherwise defined
T	statistical averaging time; sec
t	time; sec
u_1, u_2	velocity of the first and second oscillators, respectively; in./sec
V_3, V	volume of the interior air; in^3
V_{rms}	root mean square value of speaker input voltage; volts
w	shell displacement; in.
$\underset{\sim}{x}, \underset{\sim}{x}', \underset{\sim}{x}'', \underset{\sim}{x}_1, \underset{\sim}{x}_2$	two-dimensional position vectors on shell surface, e.g., specified by (a, θ_1, x_1), etc.

LIST OF SYMBOLS (Cont'd)

$\lvert \underline{x}_1 - \underline{x}_2 \rvert$	distance between point at $\underline{x}_1$ and $\underline{x}_2$; in.
Z_m, Z_r	impedance of the m^{th} shell mode and r^{th} air mode, respectively; $(rad/sec)^2$
a_k	k^{th} input power correction factor; (non-dimensional)
β_m, β_r	damping coefficient of the m^{th} shell mode and r^{th} air mode, respectively; rad/sec
$\beta_m\theta_m, \beta_r\theta_r$	power supply per unit mass to the m^{th} shell mode and r^{th} air mode, respectively; $(in^2/sec^2)/in.$
δ_{mn}, δ_{rk}	Kronecker delta; unity when m = n or r = k, otherwise zero
ϵ_r, ϵ_m	constants related to the r^{th} air mode and m^{th} shell mode (non-dimensional)
η_2, η_3	loss factor in shell and in the interior air, respectively; (non-dimensional)
η_{23_s}, η_{21_s}	coupling loss factor between shell and interior air and that between shell and exterior air, respectively, for the s-type mode
θ_1, x_1	integration limit of area A'
θ'_m, θ'_r	a generalized "temperature" or energy level per unit mass; in^2/sec^2
ν_e	Poisson's ratio for elastic shell
ν_v	Poisson's ratio for viscoelastic shell
ρ_0	density of the air medium; $(lb\text{-}sec^2)/in^4$
$\rho_s h_s$	mass per unit area of the shell; $(lb\text{-}sec^2)/in^3$
$\underline{r}, \underline{r}_1, \underline{r}_2$	three-dimensional position vectors in the interior air space
ϕ_m, ψ_r	m^{th} shell normal mode and r^{th} air normal mode

LIST OF SYMBOLS (Cont'd)

ϕ_{mn}, ω_{mn}	shell normal mode and natural frequency of m^{th} and n^{th} axial and circumferential wave number, respectively; non-dimensional and rad/sec, respectively
$\psi_r(\underline{\tau}), \psi_r(\underline{x})$	r^{th} air normal mode in space and on a shell, respectively
ψ, ϕ	a generalized fluid displacement and the velocity potential
$\omega_b, \Delta\omega_b$	center frequency and bandwidth of the b^{th} frequency band; rad/sec and rad/sec
$\omega_c, \omega_0, \omega$	center frequency of the frequency band; rad/sec
ω_m, ω_r	m^{th} and r^{th} shell and air natural frequencies, respectively; rad/sec
ℓ, h	length and width of an "equivalent rectangular" plate for the shell
$\Delta f, \Delta\omega$	frequency band; Hz and rad/sec, respectively

SUBSCRIPTS, SUPERSCRIPTS, AND OTHER NOTATION

$< >$	time average
$( )_s$	s = AF, AS, NR modes, respectively, or for the shell when ( ) is the same for all these modes
$(\omega, \Delta\omega)$	frequency band centered at ω of bandwidth $\Delta\omega$
$\hat{( )}$	amplitude of ( )
$\dot{( )}$	time derivative of ( )
$( )_m$	( ) related to the m^{th} shell mode
$( )_r$	( ) related to the r^{th} air mode
$\int_A, \int_V$	integration over the vibrating shell area, A, and the air volume, V, respectively

SUBSCRIPTS, SUPERSCRIPTS, AND OTHER NOTATION (Cont'd)

$(\ )^*$	complex conjugate of ( )
Re( )	real part of ( )
$\overline{(\ )}^{\omega,\Delta\omega}$	average over $(\omega, \Delta\omega)$
$\overline{(\ )}^{N_r(\omega)}$	average over total air modes in $(\omega, \Delta\omega)$
$(\tilde{\ })$	Fourier transform of ( )
AF, AS, NR	related to acoustically fast, acoustically slow, and non-radiating modes
$(\ )_{NG}$	related to noise generator
$\overline{(\ )}^{r}$	average over radial distance, r

INTRODUCTION

Determination of the response of elastic structures to distributed random pressures is of fundamental concern in many engineering applications. It assumes particular significance in aerospace environments where acoustical energy from several sources[1] exerts a profound influence on the dynamic response of the structure, as well as on its interior components. These pressures are usually random in time and are spatially distributed in a manner which is dependent on the phase of the launch trajectory. In general, the spatial distribution is not random, but is a deterministic function which varies with the speed of the vehicle, as well as with its position in the trajectory.

Barnoski, et al.[2] have reported a recent survey of the various methods available for the prediction of structural response to random excitation. However, most of these methods involve the application of empirical results extrapolated from previously available experimental data. The modal, or classical method, and the statistical energy method are two that are more generally applicable, and are developed with at least some mathematical rigor. Nevertheless, both methods involve numerous simplifying assumptions which inevitably limit their use in a given practical case.

The modal method is generally considered to be useful in low frequency regions which include low modal density. Some of its limitations for application to the case of a cylindrical shell excited by random acoustic excitation were determined in the initial phase[3] of the present program. The results

of the remaining work, which are reported herein, represent an investigation of the response of the same basic cylindrical configuration over much wider frequency ranges which include high modal density and significant acoustic radiation. Two different formulations of the statistical energy method are employed for prediction and compared with the results of experiments which were designed to determine the practical applicability of this method. Thus, it is applied to a problem involving an excitation pressure having a space-wise deterministic distribution, rather than a diffuse sound field, in order to simulate, at least qualitatively, a form of the acoustic fields encountered in space vehicle applications.

EXPERIMENTAL ANALYSIS

Description of Physical System

Various previous investigations[4,5] have considered the response of a cylindrical shell to a spatially diffuse random acoustic excitation. For the present case, a non-diffuse excitation is desired. Therefore, the physical arrangement depicted in Figure 1 was selected. This is a similar system to that which was utilized in our previous effort[3], except that more elaborate calibration procedures are necessary at higher frequencies, and the cylinder was capped in this case. The acoustical speaker was chosen to provide a reasonably effective area of excitation, yet small enough to minimize the computations required to obtain theoretical numerical results. A photograph of part of the actual apparatus is shown in Figure 2. The entire apparatus, which was designed to perform several related experiments, was composed of six parts: test fixture, excitors, excitation sources, transducers, analyzers, and recording devices, all of which are shown in the schematic of Figure 3.

The test fixture was a thin-walled aluminum cylinder whose physical properties are given in Table I. This cylinder was bolted (by a welded-on ring flange) to a heavy steel plate at its bottom and similarly to a heavy 3/4-inch aluminum disk plate at its top, which put the cylinder in an enclosed and nearly fixed-end configuration. Wood baffle plates of 1/4-inch thickness separated the interior space from the end plates. An isomode pad was used to cushion the steel base plate on crossed steel I-beams, which

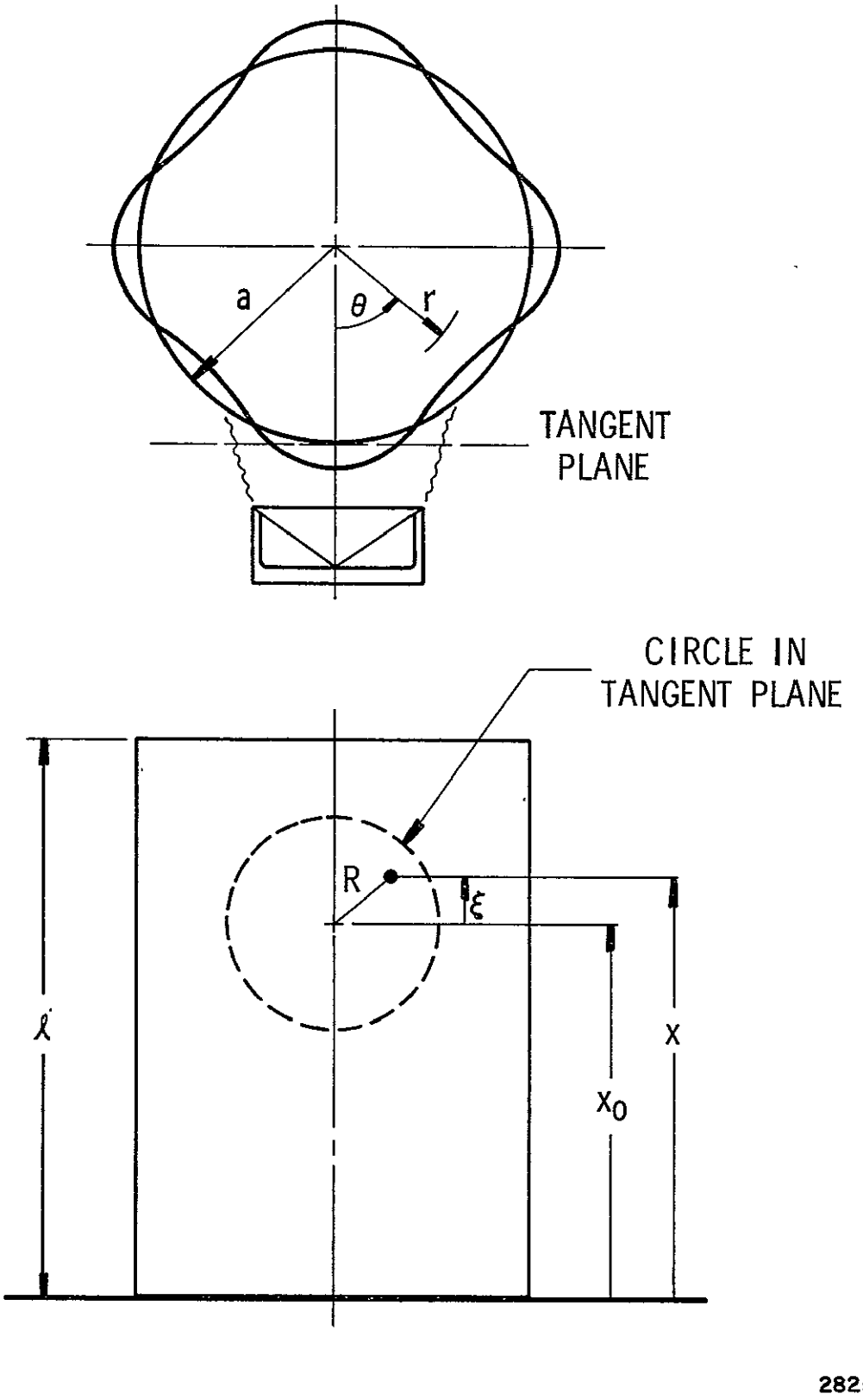

Figure 1. Coordinate System

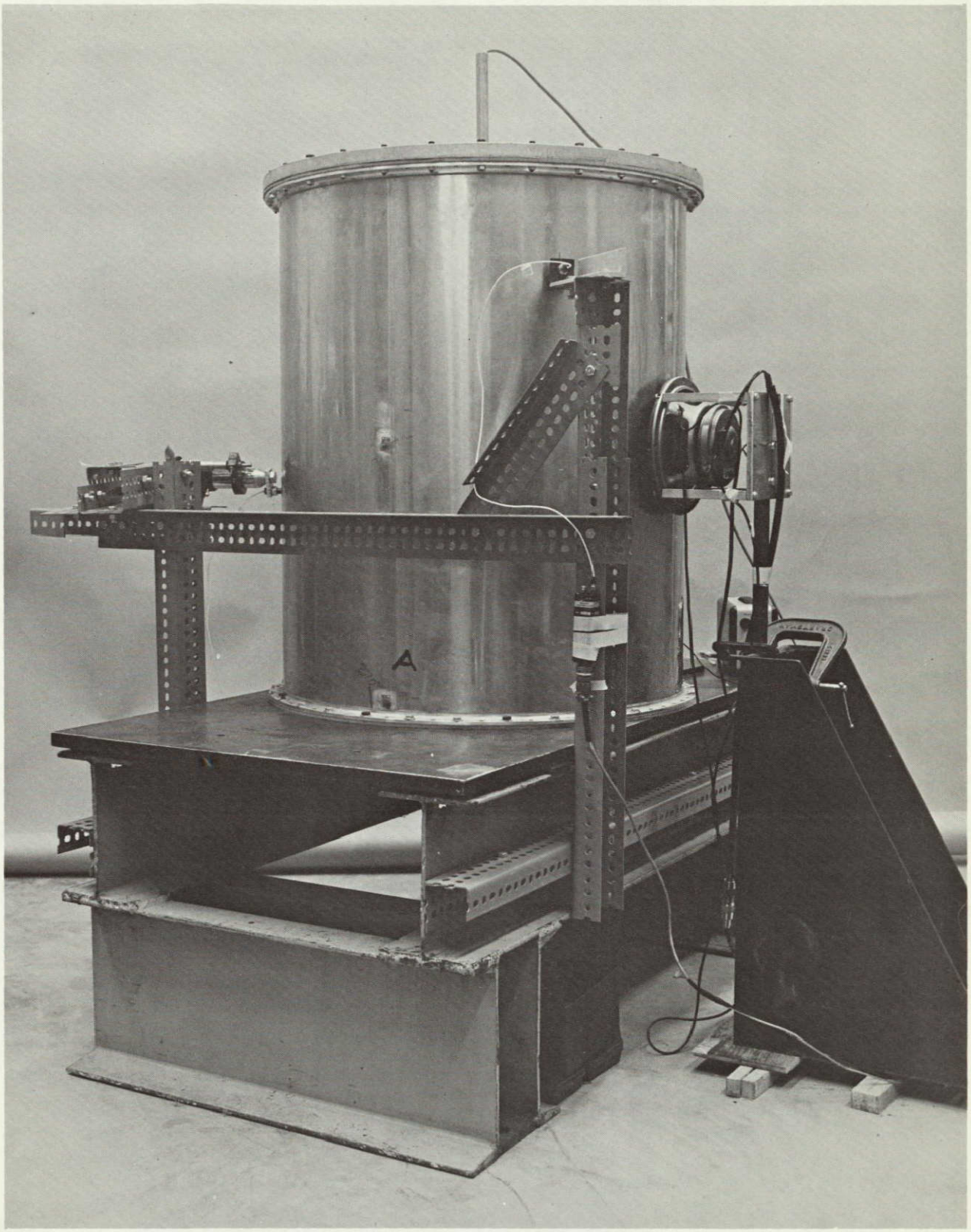

Figure 2. Photograph Of Apparatus

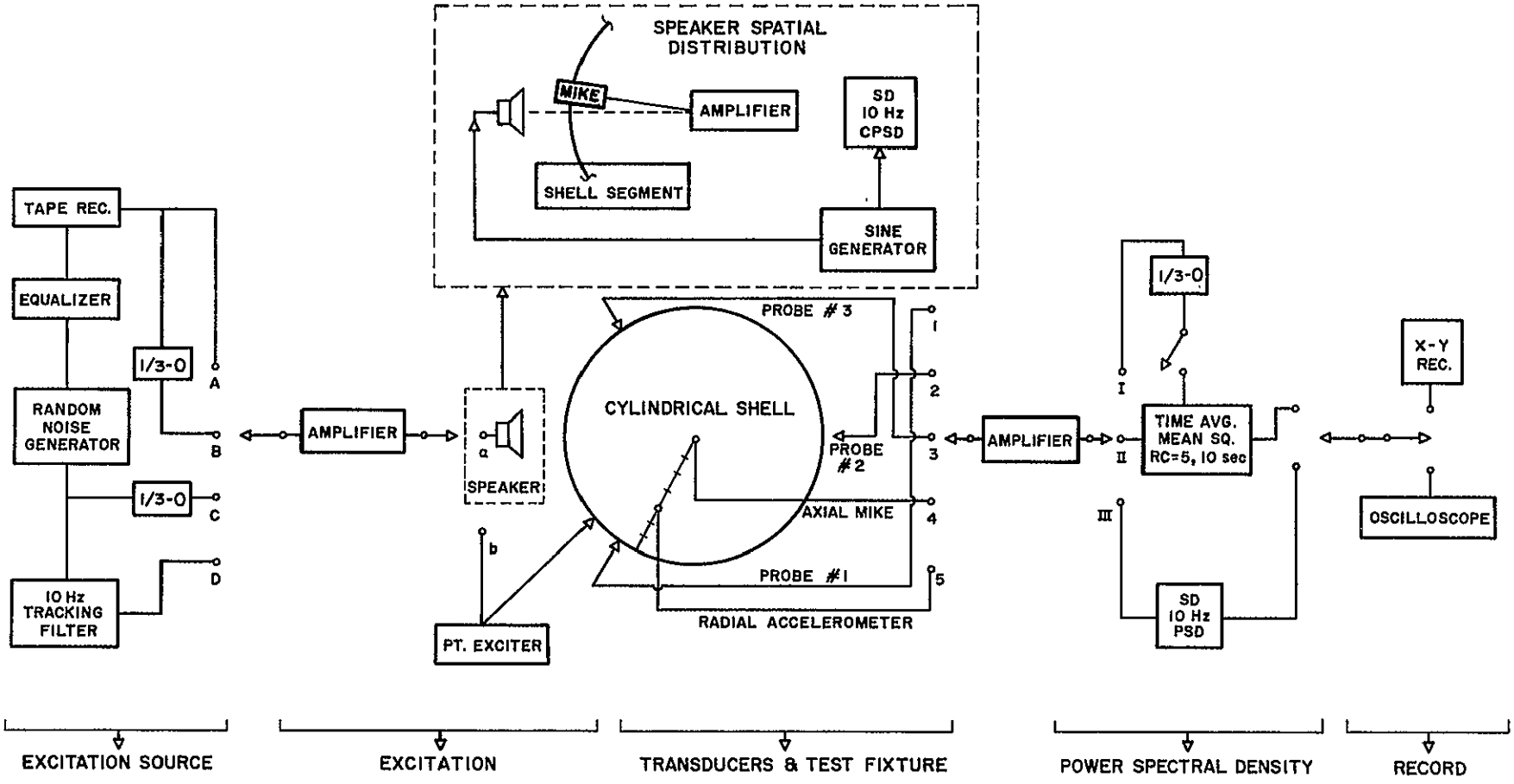

Figure 3. Schematic Of Instrumentation

TABLE I. PROPERTIES OF TEST CYLINDER

ρ_s	=	2.59×10^{-4} lb-sec^2/in^4
h_s	=	0.020 in.
a	=	12.42 in.
ℓ	=	30.0 in.
f_r	=	2,640 Hz
f_c	=	23,300 Hz

Material = 6061-T6 Aluminum.

in turn rested on a concrete floor. The function of the isomode pad was to eliminate excitation of the cylinder through floor vibrations. A 3/4-inch hole was drilled through the center of the aluminum top plate of the test fixture to allow access to the interior of the cylinder, so that a study of the characteristics of the internal acoustic field was possible. Figure 2 is a photograph of the test fixture in the configuration in which the acoustical speaker was used as an excitor.

Two excitors were used. The primary one was an 8-inch "hi-fi" loudspeaker which was mounted in relation to the cylinder as described by the coordinate system in Figure 1, where x_0 = 15.00 inches. The plane defined by the edges of the speaker cone was parallel to and 0.85 inch from the tangent plane to the cylinder at the excitation center (r, θ, $x = a$, 0, x_0). The acoustical speaker was mounted independent of the test fixture, to the concrete floor by a steel support as seen in Figure 2. Measurement of the properties of the acoustic field generated by the loudspeaker will be described under Calibration Procedures.

The secondary excitor was a small magnet whose pole pieces were parallel and close together (approximately 0.25 inch). The coil of this magnet could be driven by an AC power source and the pole pieces could be placed in close proximity to the cylinder wall (approximately 0.10 inch). The interaction of eddy currents produced locally in the cylinder wall and the AC magnetic field effected a remote point excitation of the cylinder at twice the frequency at which the magnet was driven. This magnet was

used in only a few experiments which were designed to identify acoustic modes excited within the interior air cavity.

The excitation sources were the signal generators used to drive the excitors through a 200-watt MacIntosh power amplifier. There were essentially four different excitation sources; a sine-wave generator and three sources of random noise. The first random source was created by taking the output of an Elgenco gaussian random noise generator, equalizing by means of LTV peak-notch filters to compensate for the frequency response characteristics of the loudspeaker, and taping the result on an Ampex FR-1800L tape recorder for frequencies below 2.5 kHz. This 60-Hz to 2.5-kHz nominally equalized random noise signal on tape was called our wide-band excitation. The second random source was formed by filtering this wide-band taped signal through 1/3-octave filters, having standard center and half-power frequencies as defined in Table II. The taped signal was played through these filters one at a time using filters from 100-Hz through 2-kHz center frequencies. This was called our 1/3-octave equalized signal. The third random source was the Elgenco random noise generator filtered directly by the 1/3-octave filters for center frequencies from 100 Hz to 5 kHz. This was called our 1/3-octave non-equalized signal.

Five transducers were used to measure characteristics of the cylinder under excitation. Three of these were Bentley displacement detectors located relative to coordinates of Figure 1, while values for these probe locations are given in Table III. A fourth transducer was a B&K 1/4-inch diameter microphone located at various points inside the cylinder.

TABLE II. 1/3-OCTAVE FILTER CENTER FREQUENCIES AND 1/2-POWER POINT FREQUENCIES

Filter No.	Center Frequency	1/2-Power Point Frequencies	
1	100	88	111
2	125	111	140
3	160	140	178
4	200	178	222
5	250	222	279
6	315	279	355
7	400	355	443
8	500	443	557
9	630	557	705
10	800	705	887
11	1000	887	1112
12	1250	1112	1405
13	1600	1405	1778
14	2000	1778	2220
15	2500	2220	2790
16	3150	2790	3530
17	4000	3530	4440

TABLE III. TRANSDUCER LOCATIONS

	θ	x
Probe 1	81°	7.55 in.
Probe 2	204°	12.25 in.
Probe 3	318°	24.40 in.

The fifth transducer was an Endevco accelerometer located on the top plate of the test fixture at various points along a radius at $\theta = 45°$.

Transducer signals were amplified and analyzed by three analog methods as shown in Figure 3: (1) The signals were fed directly into a Ballantine voltmeter which has an output proportional to the mean square of its input, and this output was time-averaged for 5 to 10 seconds as desired. (2) The signals were filtered with the 1/3-octave filters and then the time-averaged mean square signal was obtained with the Ballantine meter. (3) The signals were fed into a Spectral Dynamics SD-101 tracking filter with a 10-Hz bandwidth and then into an SD-109 Power Spectral Density (PSD) Analyzer with variable RC. The latter system allowed relatively narrow band analysis. The results of all analysis methods were recorded either on X-Y recorders or on oscilloscope camera film.

Calibration Procedures

In order to define the spatial distribution of the acoustic field, calibrations were performed on the speaker prior to its use in the experiments. The instrumentation setup for the speaker calibration is seen in block diagram form (within the dashed-line area) in Figure 3. The B&K microphone was mounted in a baffle which simulated a segment of the cylindrical shell of the test fixture. The axis of the highly directional microphone was coincident with the shell radius, and the entire shell segment could be rotated on this radius. Thus, the microphone could effectively measure the acoustic field pressure on the cylindrical surface at points referenced to corresponding projected points which lay in a plane

tangent to the segment at its intersection with the speaker cone axis. A photograph of the speaker and cylinder segment setup may be seen in Reference 3.

Mapping of the acoustic field spatial distribution was done for the center frequencies of the 1/3-octave filters only, and was thus considered to be an average over each respective band. The field was found to be essentially symmetric with the axis of the speaker cone; thus, only one coordinate (R in Figure 1) was necessary to designate a point located in the tangent plane, but coincident with a point on the shell at which the sound pressure was measured with the microphone.

In order to obtain the field distribution, a cross-spectral density was computed between the pressures measured at R = 0 and those for various $R \neq 0$. These data were found to consist of real (CO) and imaginary (QUAD) parts, and were completely deterministic in space as was expected. Data were taken relative to CO of CPSD = 1.0 for R = 0. The general empirical equation

$$k_R = \exp(-A_0 R^{B_0}) \cos(\pi R/P_0) \tag{1}$$

was found to fit the CO data well for various values of A_0, B_0, and P_0, which were dependent on the center frequencies of the 1/3-octave filters. The empirical equation

$$k_I = D_0 \cos(\pi R/G_0) - B_0 \tag{2}$$

fit the data for the QUAD part where the constants D_0, E_0, and G_0 also were dependent on the center frequencies of the 1/3-octave filters. Values of these parameters for various center frequencies are given in Appendix A. Relative CO and QUAD plots as a function of R are given in Figures 4a and 4b.

In order to provide a complete absolute calibration of the speaker field, the above relative distribution must be combined with a power spectral density measurement at R = 0. For this, the ratio of the time-averaged acoustic power in RMS psi squared to the RMS volts squared of signal across the speaker terminals was measured for the three different random excitation sources at R = 0. For the cases of 1/3-octave equalized and non-equalized excitation sources, the microphone and speaker terminal signals were measured directly by the time-averaged mean square Ballantine apparatus. For the case of the wide-band excitation source, the microphone and speaker terminal signals were analyzed with the 1/3-octave filters and the resultant signals measured with the time-averaged mean square Ballantine apparatus. A PSD plot of the speaker output in psi^2/Hz for the constant wide-band input to the speaker terminals (R = 0) is shown in Figure 5. This plot was obtained with the use of the Spectral Dynamics equipment using a 20-Hz filter, RC = 3 sec. Circled points on the plot at the 1/3-octave filter center frequencies were obtained from the calibration constant for the speaker by using the 1/3-octave equalized excitation source. The averaging effect of these wider-band filters compared with the 20-Hz filter may be clearly seen. A list of the speaker calibration constants is given in Appendix B.

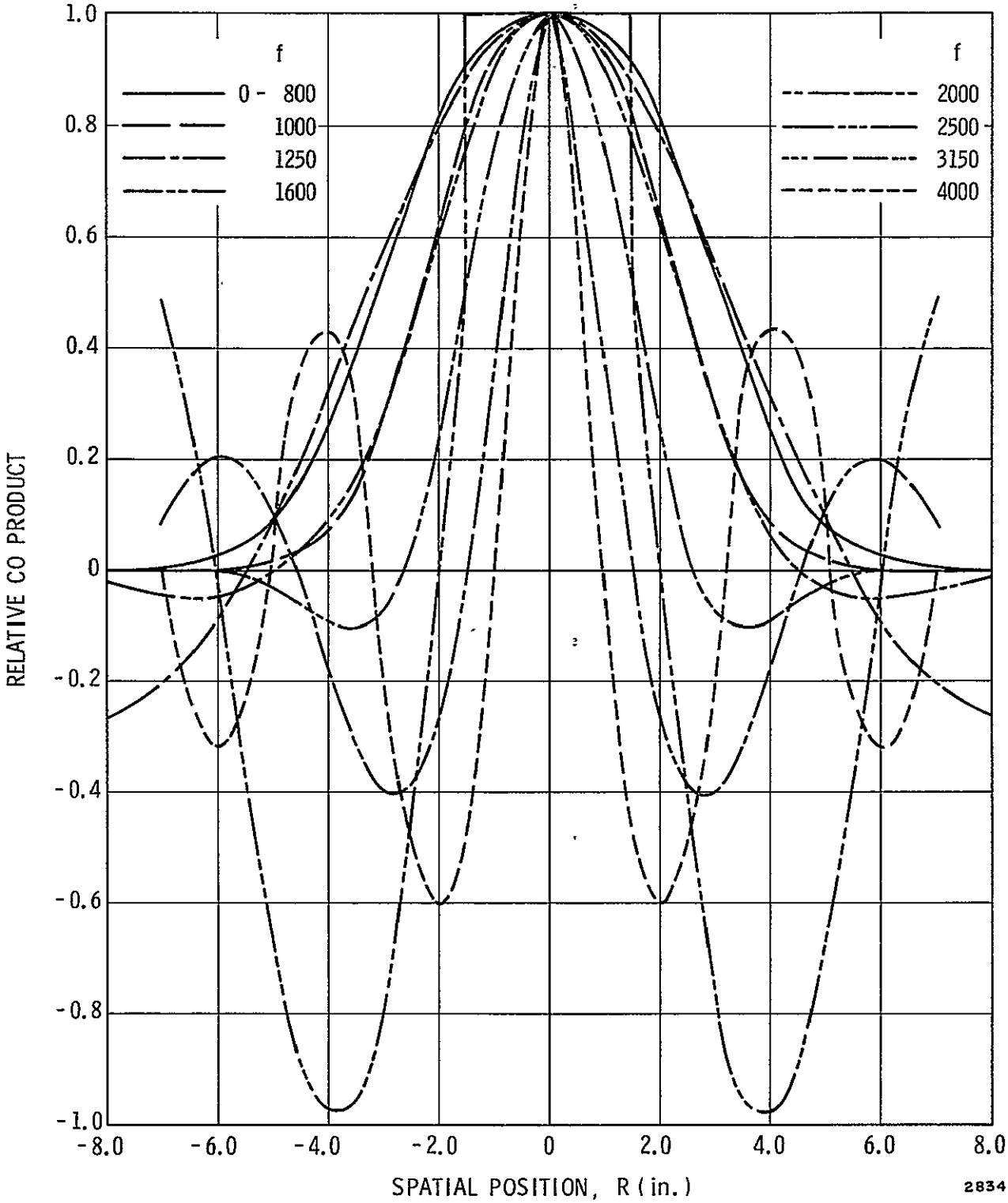

Figure 4a. Spatial Distribution Of Acoustic Field (Real Part)

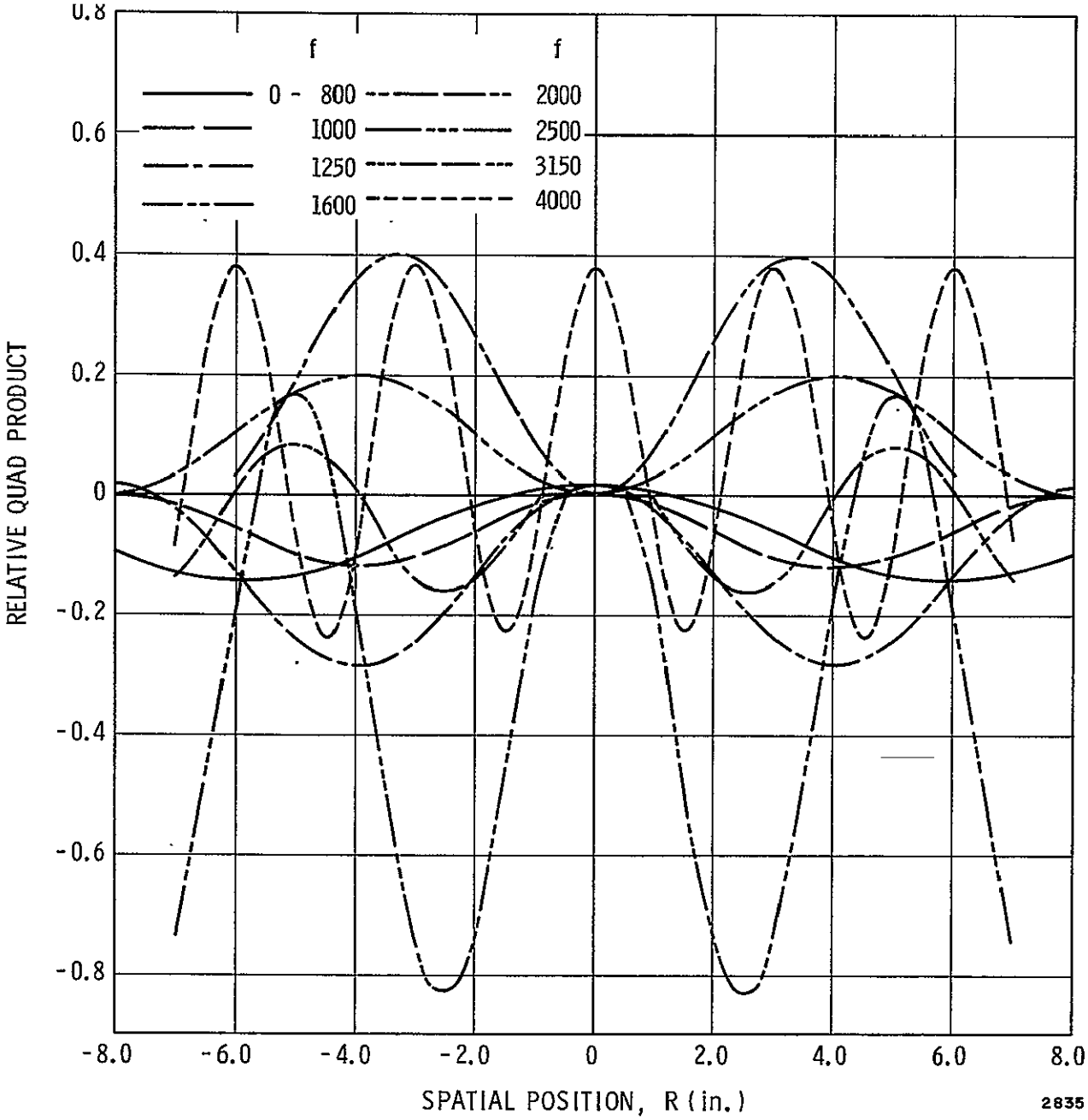

Figure 4b. Spatial Distribution Of Acoustic Field (Quadrature Part)

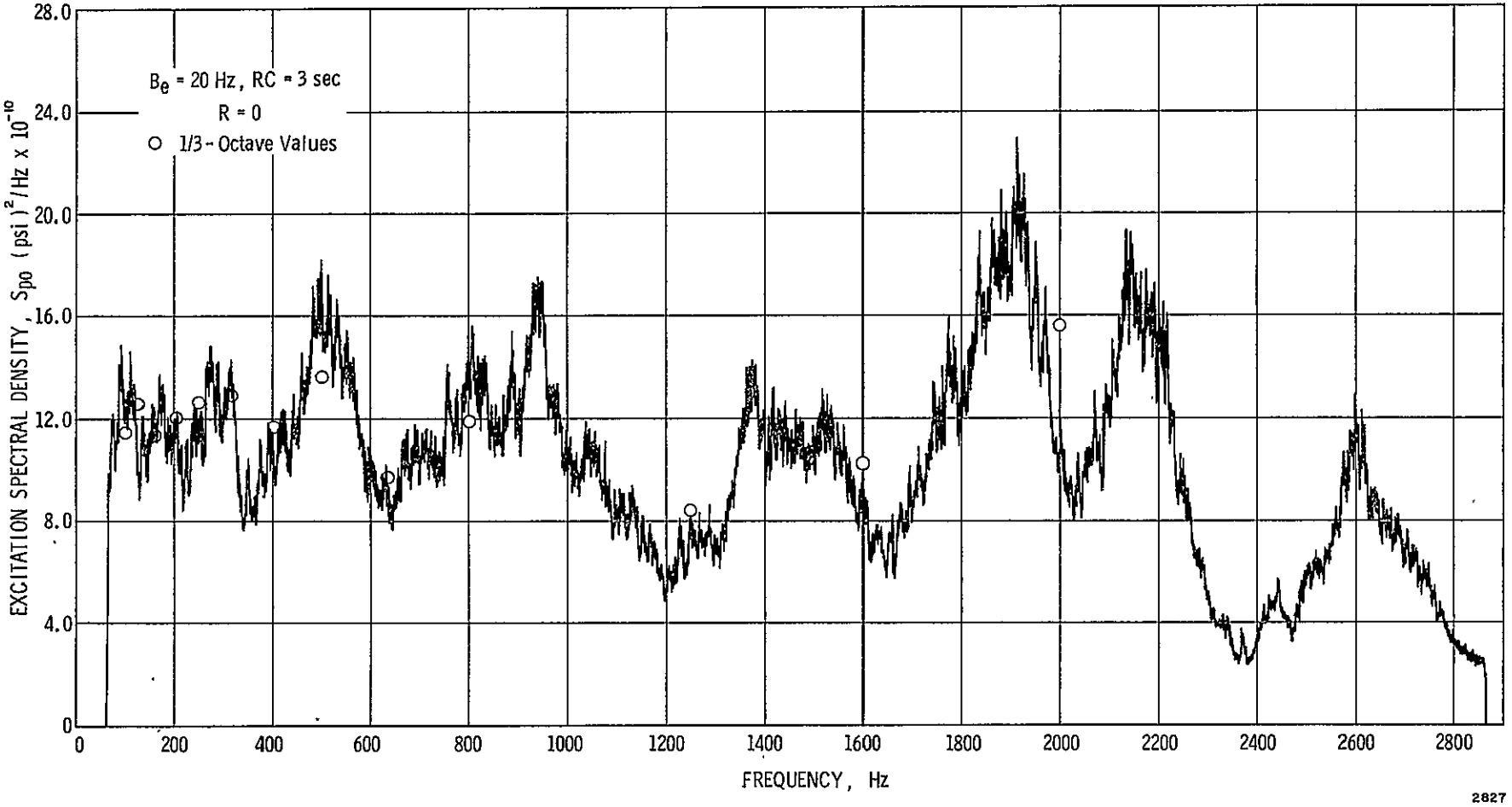

Figure 5. Power Spectrum For Broad - Band Excitation

The Bentley displacement probes were calibrated at locations on the cylinder wall of the test fixture with the use of a micrometer head to measure static distance to 10^{-4}-inch accuracy. However, this linear range about the operating point used during the experiments was more than sufficient to insure good dynamic results to 10^{-6}-inch accuracy. The axial microphone was calibrated with a B&K 124-dB audio pressure standard. The accelerometer was calibrated with a Kistler Model 808K/561T quartz vibration calibration standard.

Experiments Performed

Three major experiments were performed in relation to shell response, along with additional supporting experiments. For the appropriate instrumentation setup and the given switch locations, refer to Figure 3. The major experiments involved measurements of shell displacement and interior air pressure response for the following conditions:

(1) Wide-band equalized excitation source--the loudspeaker was used as the exciter, and the output of the proximity probes was analyzed with the 1/3-octave filters (switch locations A, a, 1-4, I) and the Ballantine meter.

(2) 1/3-octave equalized excitation source--the loudspeaker was used as the exciter, and the output of the proximity probes was analyzed with the Ballantine meter directly (switch locations B, a, 1-4, II).

(3) 1/3-octave non-equalized excitation source--the loudspeaker was used as the exciter, and the output of the proximity probes was analyzed with the Ballantine meter directly (switch locations C, a, 1-4, II).

Additional supporting experiments were also performed. Top plate accelerations were measured at points along a radius for 1/3-octave

non-equalized excitation (switch locations C, a, 5, II). A 10-Hz resolution PSD of the outputs of proximity probe No. 2 and the microphone was obtained when using random noise through a 10-Hz tracking filter as an excitation source (switch locations D, a, 3-4, III). Damping measurements for the tank were obtained by means of sine wave excitation with the speaker and by observing the probe outputs on oscilloscope records. Both 1/2-bandwidth and free-decay methods were utilized. Not all components for these experiments are shown in Figure 3. Finally, some cursory observations of displacement probe and microphone outputs were made with excitation by means of the electromagnetic coil. This method was used to identify low frequency air modes as symmetrical.

THEORETICAL ANALYSIS

General Modal Relationships

Before proceeding to discuss the details of the statistical energy method as applied to the vibration of a cylinder in air, first it is necessary to recognize the existence of different modal groups over various parts of a wide frequency band. Some of the principles set forth by Manning and Maidanik[6] will be utilized for this purpose.

Figure 6 shows a diagram which depicts many of the modes of the present cylinder over a wide frequency range. The general relationship utilized for calculating these modes is

$$\nu = \left\{\beta_0^2 a^4[(n/a)^2 + (m_0\pi/\ell)^2]^2 + (1 - \nu_e^2)(m_0\pi/\ell)^4/[(n/a)^2 + (m_0\pi/\ell)^2]^2\right\}^{1/2} \tag{3}$$

where

$$\nu = f/f_r, \qquad \beta_0^2 = (h_s^2/12a^2), \qquad m_0 = m + 0.2$$

$$f_r^2 = \frac{c_\ell^2}{4\pi^2 a^2}, \qquad c_\ell^2 = E/[\rho_s(1 - \nu_e^2)]$$

Note, that following Arnold and Warburton[7], an effective axial wave number m_0 is utilized for the present case of a cylinder with partially fixed ends. For convenience, the vertical frequency scale of Figure 6 has been divided into the standard 1/3-octave bands at the 1/2-power point frequencies previously given in Table II.

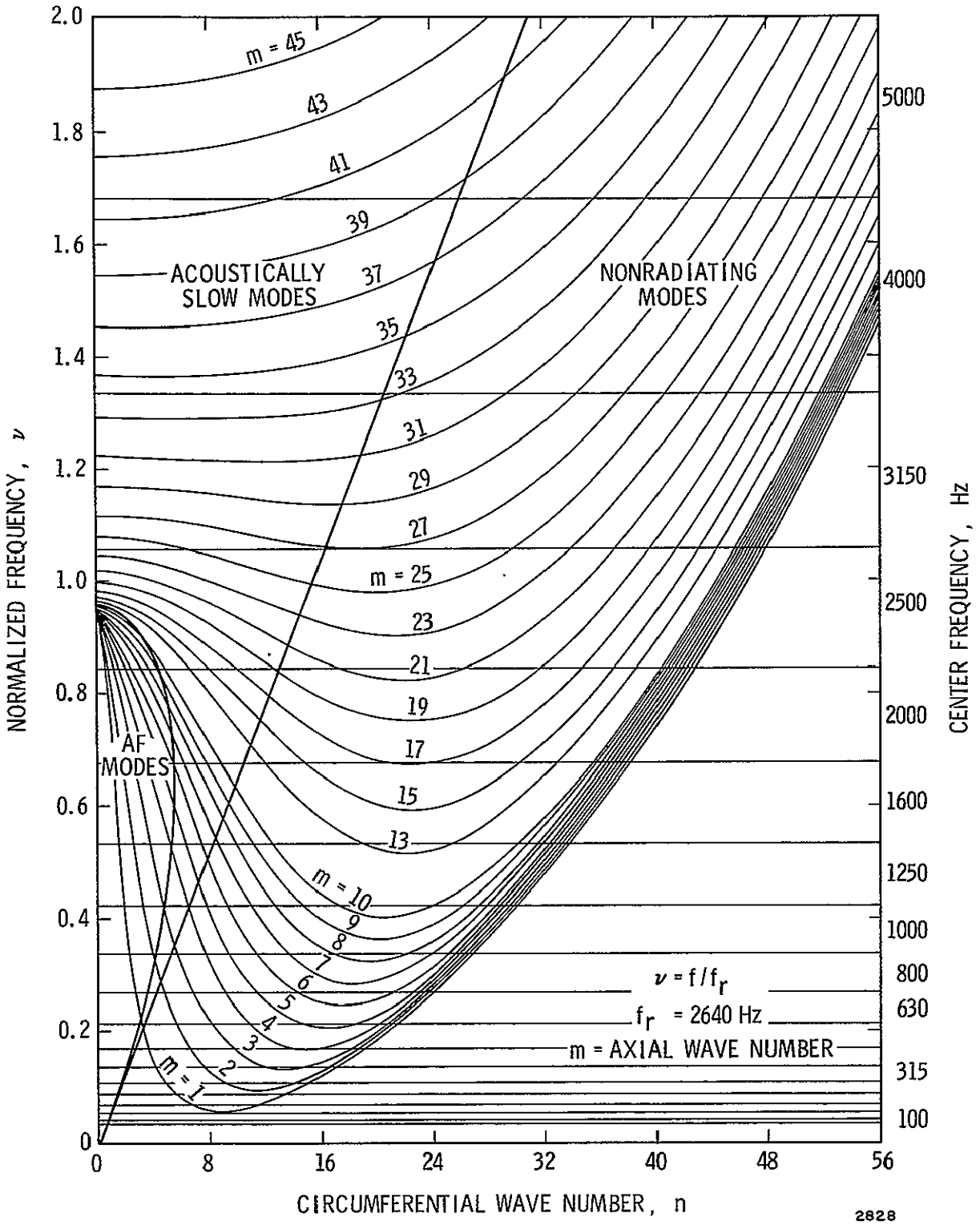

Figure 6. Modal Diagram For Cylindrical Shell

The modes of the cylinder have been separated into three distinct groups representing non-radiating (NR), acoustically slow (AS), and acoustically fast (AF) modes. Non-radiating and acoustically slow modes are separated by the straight line

$$\nu = (c_0/c_\ell)n \tag{4}$$

while acoustically slow and acoustically fast modes are approximately separated by the curve

$$n = (c_\ell/c_0)\nu \, \mathrm{Re}\left[\left\{(1 - \nu_e^2)^{1/2} - \nu[1 - (\nu/\nu_c)^2]^{1/2}\right\}^{1/2}\right] \tag{5}$$

where

$$\nu_c = f_c/f_r, \quad f_c = \frac{c_0^2}{2\pi(D/\rho_s h_s)^{1/2}}, \quad D = \frac{Eh^3}{12(1 - \nu_e^2)}$$

It should be recognized that additional, acoustically fast modes occur at higher frequencies outside the present range of interest.

Modal density for the cylinder obviously becomes quite high within the frequency range considered in Figure 6. For the sake of information, a modal density count for total modal density and density of acoustically fast modes are compared with theoretical predictions in Figure 7. Theoretical values are based on Eqs. (67) and (68) of Bozich and White[5], which are valid for a simply-supported cylinder. There is obvious disagreement for the total modal density which may result from the extrapolation of Eq. (3) to the case of a cylinder with nearly fixed ends. Therefore, in the present work, modal density was based on actual modal count obtained from Figure 6

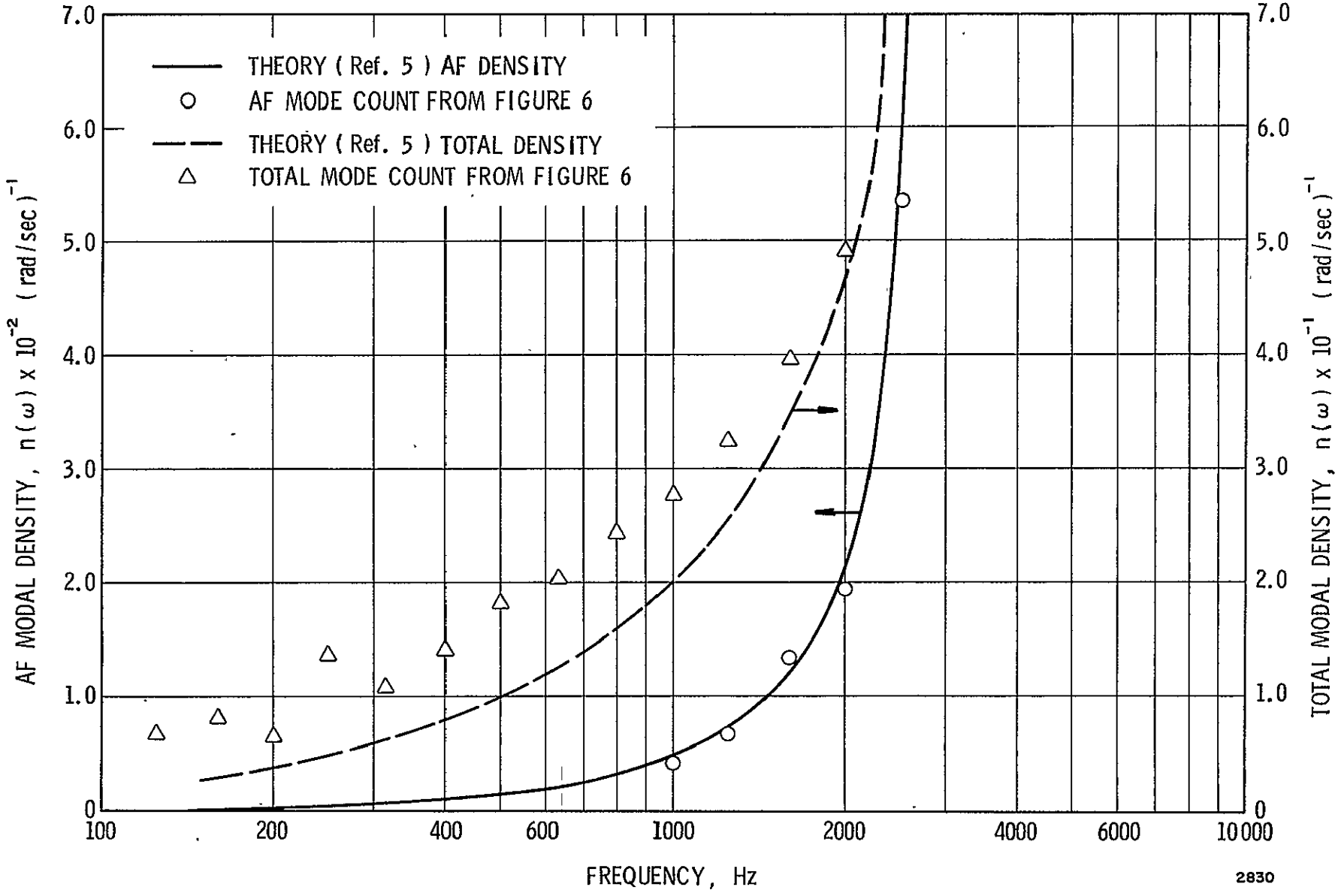

Figure 7. Modal Density For Cylindrical Shell

in order to be consistent. Thus, for each 1/3-octave band, the number of each type of modes I_{2AF}, I_{2AS}, and I_{2NR} were counted directly from Figure 6, along with Eqs. (4) and (5).

Power Balance Equations

General Concepts

The general formulation of the statistical energy analysis involves equations for power flow in and out of designated subgroups of a system. Barnoski, et al.,[2] and Ungar[8] have presented recent summaries of the fundamentals of the method and are careful to point out the existence of numerous limitations on its use. Further discussion of these limitations has been presented by Zeman and Bogdanoff[9]. For our purpose here, it will be convenient to repeat the assumptions given by Reference 2 as required in the application of the method:

(1) Modes of each substructure of interest must be grouped into similar sets.

(2) Coupling between modes in a group is negligible.

(3) Coupling between groups is conservative.

(4) Modal damping is light and modal response is mostly resonant.

(5) The power spectrum of force is approximately constant over the bandwidth of interest.

(6) Kinetic energy is evenly divided among modes in a set.

(7) Kinetic energy in coupling must be small compared to modal kinetic energy.

(8) The coupling factors between modes is constant and not strongly frequency dependent near the resonance condition.

Use of these assumptions will become apparent in the development that follows.

Detailed Derivation

One possible form of power balance equations for the vibration of a cylinder in air has been presented by Conticelli[10] and Bozich and White[5]. However, their equations do not directly contain terms which allow for a non-diffuse excitation, or for non-radiating modes. Therefore, we will first present a similar set of equations which do account for such additions. These equations will be referred to as the separate group theory, for reasons which will become obvious. Then, as a result of discrepancies which resulted between this theory and measured values in part of the frequency range, a second, slightly modified theory is developed. It will be referred to as the percentage theory. In particular, the non-interaction between AF, AS, and NR structural modes of the shell is considered in an alternate manner. Both, however, are slightly different modifications of the same basic statistical energy theory. The development will proceed from several earlier references on the subject.

For two normalized linear oscillators[11] having instantaneous velocities u_1 and u_2, power balance equations can be written as

$$\beta_1\langle u_1^2\rangle - g_{12}(\theta_1 - \theta_2) = \beta_1\langle u_1^2\rangle - r_{12}[\langle u_1^2\rangle - \langle u_2^2\rangle] = \langle f_1 u_1\rangle \quad (6)$$

$$\beta_2\langle u_2^2\rangle - g_{21}(\theta_2 - \theta_1) = \beta_2\langle u_2^2\rangle - r_{21}[\langle u_2^2\rangle - \langle u_1^2\rangle] = \langle f_2 u_2\rangle \quad (7)$$

The first term in Eq. (6) represents the average internal dissipation. β_1 is a normalized damping coefficient of the first oscillator, and θ_1 is the average energy (per mode) of the first oscillator $\langle f_1 u_1 \rangle / \beta_1$. The second term represents the power flow from mode 1 to mode 2; g_{12} is the power flow coefficient; and r_{12} is the coupling coefficient between mode 1 and mode 2. The extreme right-hand side of Eq. (6) represents the work done per second, or the input power on mode 1. The terms in Eq. (7) have similar meanings. For "gyroscopic" coupling, which holds[11] for shell-air coupling $g_{12} = g_{21}$, $r_{12} = r_{21}$, and the dissipation in the system is independent of the coupling which is, in this sense, conservative. More general coupling equations will be discussed later.

For our present problem, the above equations are extended to groups of modes so that the subscripts 1, 2, and 3 are used for the outside air, the cylindrical shell, and the interior air, respectively. However, group 2 is further separated into NR, AS, and AF modes. In the separate group theory, essentially five groups are then defined, i.e., 1, 2NR, 2AS, 2AF, and 3. In this case, we may write Eqs. (6) and (7) accordingly as power balance (per unit bandwidth) equations. For the cylinder

$$\omega\eta_2 E_{2AF} + \omega\eta_{23AF} n_{2AF} \left(\frac{E_{2AF}}{n_{2AF}} - \frac{E_3}{n_3} \right) + \omega\eta_{21AF} n_{2AF} \frac{E_{21AF}}{n_{2AF}} = P_{2AF}^{IN} \qquad (8)$$

$$\omega\eta_2 E_{2AS} + \omega\eta_{23AS} n_{2AS} \left(\frac{E_{2AS}}{n_{2AS}} - \frac{E_3}{n_3} \right)$$

$$+ \omega\eta_{21AS} n_{2AS} \frac{E_{2AS}}{n_{2AS}} = P_{2AS}^{IN} \qquad (9)$$

$$\omega\eta_2 E_{2NR} = P_{2NR}^{IN} \qquad (10)$$

Note that for non-radiating (NR) modes the acoustic coupling is considered negligible. Similarly, for the interior air

$$\omega\eta_3 E_3 - \omega\eta_{23AF} n_{2AF} \left(\frac{E_{2AF}}{n_{2AF}} - \frac{E_3}{n_3} \right)$$

$$- \omega\eta_{23AS} n_{2AS} \left(\frac{E_{2AS}}{n_{2AS}} - \frac{E_3}{n_3} \right) = 0 \qquad (11)$$

A similar equation for coupling to the external air is not required since it is assumed to be of infinite extent. These are the governing equations for the separate group theory.

Now, consider a slightly alternate method of arranging the governing equations. Consistent with the concepts of the statistical energy theory, the modes of each separate medium (1 or 2 or 3) are assumed to possess approximately the same energy level. In particular, we shall assume that the shell structural modes, AF, AS, or NR are approximately of the same energy so the structural coupling between these modes can be neglected. We have:

$$\langle u_2^2 \rangle \Rightarrow \frac{E_2}{n_2} = \frac{E_{2AF}}{n_{2AF}} = \frac{E_{2AS}}{n_{2AS}} = \frac{E_{2NR}}{n_{2NR}} \tag{12}$$

$$\langle u_3^2 \rangle \Rightarrow \frac{E_3}{n_3} \tag{13}$$

Since the exterior domain of air is assumed to be of nearly infinite extent, there is only radiation outward from the shell with negligible reflected radiation

$$\langle u_1^2 \rangle \cong 0 \tag{14}$$

The power equation of medium 1 thus is decoupled from the shell-interior-air power equations. Equations (6) and (7) yield the following average power balance equation (per unit band width) for AF, AS, and NR modes, respectively:

$$\omega\eta_2 E_{2AF} + \omega\eta_{23AF} n_{2AF} \left(\frac{E_2}{n_2} - \frac{E_3}{n_3} \right) + \omega\eta_{21AF} n_{2AF} \frac{E_2}{n_2} = P_{2AF}^{IN} \tag{15}$$

$$\omega\eta_2 E_{2AS} + \omega\eta_{23AS} n_{2AS} \left(\frac{E_2}{n_2} - \frac{E_3}{n_3} \right) + \omega\eta_{21AS} n_{2AS} \frac{E_2}{n_2} = P_{2AS}^{IN} \tag{16}$$

$$\omega\eta_2 E_{2NR} = P_{2NR}^{IN} \tag{17}$$

Similarly, the average power balance equation for the interior air modes is:

$$\omega\eta_3 E_3 - \omega\eta_{23AF} n_{2AF} \left(\frac{E_2}{n_2} - \frac{E_3}{n_3}\right)$$

$$- \omega\eta_{23AS} n_{2AS} \left(\frac{E_2}{n_2} - \frac{E_3}{n_3}\right) = 0 \qquad (18)$$

Equations (15) through (18) are the basic governing equations for the percentage method. Consider now a slight rearrangement of these equations which makes the name of the method more obvious. The total energy of the shell is

$$E_2 = E_{2AF} + E_{2AS} + E_{2NR} \qquad (19)$$

The total number of shell resonant modes per unit bandwidth is

$$n_2 = n_{2AF} + n_{2AS} + n_{2NR} \qquad (20)$$

Only reasonant modes are counted, since except at low frequencies, their contribution to energies outweighs other modes provided that they are lightly damped. If Eqs. (15) to (17) are summed (with equal weight), one obtains

$$\omega\eta_2 E_2 + \omega\eta_{23} n_2 \left(\frac{E_2}{n_2} - \frac{E_3}{n_3}\right) + \omega\eta_{21} n_2 \left(\frac{E_2}{n_2}\right)$$

$$= P_2^{IN} = P_{2AF}^{IN} + P_{2AS}^{IN} + P_{2NR}^{IN} \qquad (21)$$

where the coupling coefficients are

$$\eta_{2j} = \frac{n_{2AF}}{n_2} \eta_{2jAF} + \frac{n_{2AS}}{n_2} \eta_{2jAS}, \quad j = 1 \text{ or } 3 \qquad (22)$$

Equation (22) expresses each part of the radiation as a portion, or percent, of the total radiation. This is similar to that presented by Manning and Maidanik[6].

The determination of number of modes I_{2AF}, I_{2AS}, I_{2NR} in each given bandwidth $\Delta\omega$ centered at ω is described in the previous section. For the shell, the respective modal densities are then

$$n_{2AF} = I_{2AF}/\Delta\omega, \text{ etc.} \tag{23}$$

For the number of interior air modes, we will employ those for an equivalent rectangular room[12] (which is only an approximation for the present case)

$$n_3 = \omega^2 V_3 \Big/ (2\pi^2 c_0^3) \tag{24}$$

This expression is valid for a rectangular room at high frequencies, and is an approximation based on the more general expression, Eq. (3.4), on p. 86 of Reference 13. Note the difference in notation, and that a differentiation needs to be performed to get Eq. (24).

The space-average generalized displacement for sound waves in air is[11]

$$\psi = \frac{\phi}{c_0} \tag{25}$$

where ϕ is the space-averaged velocity potential, while, for small periodic disturbances, the space-averaged pressure is:

$$p \cong -\rho_0 \frac{\partial \phi}{\partial t} = \rho_0 \omega \hat{\phi} \sin(\omega t); \quad \phi = \hat{\phi} \cos(\omega t) \tag{26}$$

Thus,

$$E_3 = \rho_0 V_3 \langle \dot{\psi} \rangle^2 / \Delta\omega = \frac{S_{p3}(\omega) V_3}{\rho_0 c_0^2} \tag{27}$$

as

$$\langle p^2 \rangle_{\omega, \Delta\omega} \equiv S_{p3}(\omega) \Delta\omega \tag{28}$$

Similarly,

$$E_2 = M \langle y^2 \rangle / \Delta\omega = M\omega^2 S_y(\omega) \tag{29}$$

where y is the space-averaged shell displacement. The space-averaged pressure spectral density of the interior, S_{p3}, and the space-averaged shell displacement spectral density, S_y, can be calculated from Eqs. (27) and (29) after E_2 and E_3 are determined from the power balance equations.

Input Power

Previous investigators have usually considered only one dominant form of energy loss in impedance relationships which affect input power expressions. In the present case, where energy losses vary considerably from one part of the frequency range to another, a more accurate approximation will be derived. We start from the normalized power Eqs. (9.14b) and (9.15b) of Lyon and Maidanik[11]:

$$\beta_m \langle \dot{s}_m^2 \rangle + \sum_r^{N_r} g_{mr}(\theta_m' - \theta_r') = \beta_m \theta_m \tag{30}$$

$$\beta_r \langle \dot{q}_r^2 \rangle - \sum_m^{N_s} g_{mr}(\theta_m' - \theta_r') = \beta_r \theta_r \tag{31}$$

which are the m^{th} shell equation and r^{th} interior air equation (effects of the exterior air domain will be added later), and

$$\beta_m \theta_m = \langle F_m \dot{s}_m \rangle = \langle (M\dot{M}_m)^{-1/2} \int_A p\phi_m \, d\underline{x} \cdot \dot{s}_m \rangle \tag{32a}$$

where

$$F_m = (MM_m)^{-1/2} \int_A p\phi_m \, d\underline{x} \tag{32b}$$

and ϕ_m is the m^{th} shell normal modal function. Since

$$\langle \dot{s}_m^2 \rangle = \left(\frac{M_m}{M}\right) \langle \dot{s}_m'^2 \rangle; \qquad w(\underline{x}) = \sum_m s_m' \phi_m(\underline{x}) \left(\frac{\rho_s h_s}{M}\right)^{1/2}$$

$$\langle \dot{q}_r^2 \rangle = (\rho V \epsilon_r / M) \langle \dot{q}_r'^2 \rangle; \quad \psi(\underline{x}) = \sum_m q_r' \psi_r(\underline{\tau})$$

$$\int_A \phi_m \frac{\rho_s h_s}{M} \phi_n \, d\underline{x} = \frac{M_m}{M} \delta_{mn} = \epsilon_m \delta_{mn};$$

$$\epsilon_m = \frac{1}{4} \text{ for simply-supported panel.}\dagger$$

†Note that this expression will be only approximately correct in the present case.

$$\int_V \psi_r \psi_k \, d\underline{\tau} = V\epsilon_r \delta_{rk}; \quad \epsilon_r = \frac{1}{4} \text{ if } r \text{ and } k \neq 0$$

we have

$$E_s = \frac{1}{\Delta\omega} M \langle \dot{w}^2 \rangle = \frac{1}{\Delta\omega} \sum_m M_m \langle \dot{s}_m'^2 \rangle = \frac{1}{\Delta\omega} \sum_m M\epsilon_m \langle \dot{s}_m'^2 \rangle \tag{33}$$

$$E_a = \frac{1}{\Delta\omega} \rho_0 V \langle \dot{\psi}^2 \rangle = \frac{1}{\Delta\omega} \sum_r \rho_0 V \epsilon_r \langle \dot{q}_r'^2 \rangle \tag{34}$$

Now consider a sum of $\frac{1}{\Delta\omega} M \times$ [Eq. (30)] with respect to m. The first term yields the dissipation, $\beta_m E_s$. The second term is

$$M \sum_m \sum_r q_{mr}(\theta_m' - \theta_r') = R_{rad} \left[\sum_m \langle \dot{s}_m^2 \rangle - N_s \sum_r \frac{\langle \dot{q}_r^2 \rangle}{N_r} \right]$$

$$= \frac{R_{rad}}{M} \left[\frac{E_s}{N_s} - \frac{E_a}{N_r} \right] \tag{35}$$

Equation (35) is a generalized definition of r_{12} as a modification of the definition, Eq. (9.19) of Lyon-Maidanik[11]. The input power in the summed equation is then clearly

$$P_s^{IN} = \frac{M}{\Delta\omega} \sum_m^{N_s} \beta_m \theta_m = \frac{M}{\Delta\omega} \sum_m^{N_s} \langle F_m \dot{s}_m \rangle \tag{36a}$$

where

$$F_m = \frac{1}{\sqrt{\epsilon_m} M} \int_A p\phi_m \, d\underline{x} \tag{36b}$$

By Fourier transform, similar to p. 32 of Robson[14]:

$$x(t) = \frac{1}{2\pi} \int_{-\infty}^{\infty} \tilde{x}(\omega) e^{i\omega t} \, d\omega \tag{37}$$

$$\tilde{x}(\omega) = \int_{-\infty}^{\infty} x(t) e^{-i\omega t} \, dt \tag{38}$$

Also, the inverse transform of Eq. (8), p. 47, of Robson[14], yields

$$\langle x(t)y(t+\tau) \rangle = R_{xy}(\tau) = \frac{1}{T} \int_{-\infty}^{\infty} \tilde{x}^* \tilde{y} e^{-i\omega t} \, d\omega/2\pi \tag{39a}$$

$$\langle x(t)y(t) \rangle = R_{xy}(0) = \frac{1}{T} \int_{-\infty}^{\infty} \tilde{x}^* \tilde{y} \, d\omega/2\pi \tag{39b}$$

Consequently, for two narrow bands of width $\Delta\omega$ centered at frequencies $\pm \omega$ (as complex transforms are used), we have

$$(\Delta\omega)\hat{C}_{xy}(\omega) = \langle x(t)y(t) \rangle = \frac{1}{2\pi T} \int_{-\infty}^{\infty} \tilde{x}^*(\omega)\, \tilde{y}(\omega) \, d\omega$$

$$\cong \frac{(\Delta\omega)}{2\pi T} \left[\underbrace{\tilde{x}^*(\omega)\, \tilde{y}(\omega)}_{\omega, \Delta\omega} + \underbrace{\tilde{x}^*(-\omega)\, \tilde{y}(-\omega)}_{\omega, \Delta\omega} \right]$$

$$= \frac{(\Delta\omega)}{2\pi T} \left[\underbrace{\tilde{x}^*(\omega)\, \tilde{y}(\omega)}_{\omega, \Delta\omega} + \underbrace{\tilde{x}(\omega)\, \tilde{y}^*(\omega)}_{\omega, \Delta\omega} \right] = (\Delta\omega) \mathrm{Re} S_{xy}(\omega)$$

$$= \left(\frac{\Delta\omega}{2\pi}\right) \frac{2}{T} \mathrm{Re} \left[\underbrace{\tilde{x}^*(\omega)\, \tilde{y}(\omega)}_{\omega, \Delta\omega} \right] \tag{40a}$$

Upon division of the last term of Eq. (40a) by $\Delta\omega$, the power spectral density results:

$$S_{xx}(\omega) = \mathrm{Re}\, S_{xx}(\omega) = \frac{1}{2\pi}\left[\frac{2}{T}\overline{\tilde{x}^*(\omega)\tilde{x}(\omega)}^{\omega,\,\Delta\omega\to 0}\right] = \frac{1}{2\pi}\left[\frac{2}{T}\tilde{x}^*(\omega)\tilde{x}(\omega)\right] \tag{40b}$$

while

$$\hat{C}_{xy}(\omega) = \frac{2}{2\pi T}\,\mathrm{Re}\,\overline{[\tilde{x}^*(\omega)\tilde{y}(\omega)]}^{\omega,\Delta\omega} = \frac{1}{2\pi}\cdot\frac{2}{T}\,\mathrm{Re}\,\overline{[\tilde{x}(\omega)\tilde{y}^*(\omega)]}^{\omega,\,\Delta\omega} = \frac{1}{2\pi}\,\hat{C}_{xy}(f) \tag{40c}$$

$\hat{C}_{xy}(f)$ is the co-spectral density given in Eq. (6.51a), p. 274 of Bendat-Piersol[15]. Similarly, the quadrature spectral density is

$$\hat{Q}_{xy}(\omega) = \frac{1}{\Delta\omega}\left\langle x(t)\, y\left(t - \frac{\pi}{2|\omega|}\right)\right\rangle = \frac{i}{2\pi\Delta\omega T}\int_{-\infty}^{\infty}\tilde{x}^*\tilde{y}\,d\omega$$

$$= -\frac{1}{2\pi}\cdot\frac{2}{T}\,\mathcal{I}m\,\overline{[\tilde{x}^*(\omega)\tilde{y}(\omega)]}^{\omega,\,\Delta\omega} \tag{40d}$$

The cross-spectral density is, therefore

$$\hat{G}_{xy}(\omega) = \frac{1}{2\pi}\cdot\frac{2}{T}\,\tilde{x}^*(\omega)\tilde{y}(\omega) = \hat{C}_{xy} - i\hat{Q}_{xy} \tag{40e}$$

The Fourier transform of Eqs. (9.1a) and (9.1b) of Lyon-Maidanik[11] yields

$$\tilde{s}_m + \sum_r^{N_r}\frac{B_{rm}\tilde{\dot{q}}_r}{Z_m^*(\omega)} = \frac{\tilde{F}_m}{Z_m^*(\omega)}\,, \qquad \tilde{\dot{s}}_m = -i\omega\tilde{s}_m \tag{41}$$

$$\tilde{q}_r - \sum_m^{N_s}\frac{B_{rm}\tilde{s}_m}{Z_r^*(\omega)} = 0 \tag{42}$$

$$Z_m(\omega) = \omega_m^2 - \omega^2 + i\beta_m\omega, \quad Z_r(\omega) = \omega_r^2 - \omega^2 + i\beta_r\omega \tag{43a, b}$$

Using Eqs. (36a), (40a), (41), and (42), we have the power input

$$P_s^{IN} = \frac{M}{\Delta\omega} \sum_m^{N_s} \langle F_m \dot{s}_m \rangle = \frac{M}{2\pi} \cdot \frac{2}{T} \operatorname{Re} \sum_m^{N_s} \overline{(\tilde{F}_m^* \tilde{s}_m)}^{\omega, \Delta\omega}$$

$$= P_{I_s}^{IN} + P_{II_s}^{IN} \cong \frac{P_{I_s}^{IN}}{1 + \alpha_{rad_s}} \tag{44}$$

where α_{rad} is a radiation correction factor to be determined later. Employing "integral approximation" and residue theorem to evaluate band-average values for a lightly damped system analogous to White and Powell[16], one has

$$P_{I_s}^{IN} = \frac{M}{2\pi} \cdot \frac{2}{T} \operatorname{Re} \sum_m^{N_s} \overline{\frac{\tilde{F}_m \tilde{F}_m^*(-i\omega)}{Z_m^*(\omega)}}^{\omega, \Delta\omega} \cong \frac{M}{2\pi T} 2 \sum_m^{N_s} \tilde{F}_m^* \tilde{F}_m \left(\frac{\pi}{2\Delta\omega}\right) \tag{45a}$$

$$\cong \frac{\pi}{2Mm} A^2 n_s \langle j_n^2 \rangle_s \, S_{p_0}(\omega) \tag{45b}$$

where

$$n_s = n_{2AF}, \text{ etc.}, \quad \langle j_n \rangle_s = \langle j_n^2 \rangle_{AF}, \text{ etc.}, \text{ respectively}$$

Equation (45b) is the input derived by White-Powell[16]. Thus, the present problem requires the further evaluation of the radiation correction factor α_{rad}, which will be done shortly.

The joint acceptance in Eq. (45b) can be derived from Eqs. (45a), (32b), and (40c) as:

$$\langle J_n^2 \rangle_s = \frac{1}{A^2 I_s} \sum_m^{N_s} \int_{A'} \int_{A'} \frac{\hat{C}_{p'p''}}{S_{p_0}} \phi_m(\underline{x}') \phi_m(\underline{x}'') \, d\underline{x}' \, d\underline{x}'' \tag{46a}$$

$$= \frac{1}{A^2 I_s} \sum_m^{N_s} \int_{A'} \int_{A'} [\hat{G}_{p'p''}/S_{p_0}] \phi_m(\underline{x}') \phi_m(\underline{x}'') \, d\underline{x}' \, d\underline{x}'' \tag{46b}$$

where

$$p' = p(\underline{x}', t), \quad p'' = p(\underline{x}'', t), \quad I_s = n_s \Delta\omega \tag{47a, b, c}$$

The imaginary part of $\hat{G}_{p'p''}$ in Eq. (46b) has no effect due to its anti-symmetry with respect to $\underline{x}'$, $\underline{x}''$. Let

$$G_{p'p_0} = k_R(\underline{x}, \omega) S_{p_0}(\omega) - jk_I(\underline{x}, \omega) S_{p_0}(\omega) \tag{48}$$

It can be shown (Appendix C) that

$$\hat{C}_{p'p''} = \mathrm{Re}\, \hat{G}_{p'p''} = [k_R(\underline{x}', \omega) k_R(\underline{x}'', \omega) + k_I(\underline{x}', \omega) k_I(\underline{x}'', \omega)] \, S_{p_0}(\omega) \tag{49}$$

Consequently, for simply-supported panels and axisymmetric excitation with respect to an axis through the center of the speaker and normal to the cylindrical shell at $(r, \theta, x) = (a, 0, x_0)$

$$\langle j_n^2 \rangle_s = \frac{1}{A^2 I_s} \sum_m \sum_n (I_{mn}^2 + J_{mn}^2) \tag{50}$$

The first term in the parentheses of Eq. (50) is:

$$I_{mn} = \int_{A'} k_R(\underline{x},\omega)\,\phi_{mn}(\underline{x})\,d\underline{x} = 4a \int_0^{\theta_{mx}} \int_0^{\xi_{mx}} k_R(\xi,\,\theta,\,\omega)$$

$$\cos\left(\frac{m\pi\xi}{\ell}\right)\cos(n\theta)\,d\xi\,d\theta\,\sin\frac{m\pi x_0}{\ell} \qquad (51a)$$

where

$$\xi_{mx} = R_{mx},\quad \theta_{mx} = \sin^{-1}(R_{mx}/a) \qquad (51b)$$

$$k_R(\xi,\theta;\,\omega) \cong e^{-A_0 R^{B_0}} \cos\left[\frac{\pi R}{P_0}\right] \text{ for } R \leq R_{mx} = 8.0 \text{ inches} \qquad (51b)$$

as given previously by Eq. (1) for the present system. Note that, based on experimental data, k_R is assumed to be negligible for $R > 8.0$ inches where

$$R = \sqrt{\xi^2 + a^2 \sin^2\theta};\quad \xi = x - x_0 \qquad (51c)$$

and A_0, B_0, and P_0 are given in Appendix A. Further,

$$J_{mn} = \int_A k_I(\underline{x},\,\omega)\,\phi_{mn}(\underline{x})\,d\underline{x} = 4a \int_0^{\theta_{mx}} \int_0^{\xi_{mx}} k_I(\xi,\,\theta;\,\omega)$$

$$\cos\left(\frac{m\pi\xi}{\ell}\right)\cos(n\theta)\,d\xi\,d\theta\,\sin\left(\frac{m\pi x_0}{\ell}\right) \qquad (52a)$$

where

$$k_I(\xi,\theta;\,\omega) \cong D_0 \cos\left(\frac{\pi R}{G_0}\right) - E_0 \qquad (52b)$$

and D_0, G_0, and E_0 also are given in Appendix A.

Returning to the correction factor in Eq. (44) with the help of Eqs. (41) and (42), we have for $N_s \neq 0$ (all terms are zero when $N_s = 0$).

$$a_{rad} = \frac{+1}{\mathrm{Re}\left[\overline{\sum_{m}^{N_s} \tilde{F}_m^* \tilde{\dot{s}}_m}^{\omega, \Delta\omega}\right]} \mathrm{Re}\left\{\overline{\sum_{m}^{N_s}\sum_{r}^{N_r} \frac{B_{rm}\tilde{q}_r \tilde{F}_m^*(-i\omega)}{Z_m^*(\omega)}}^{\omega, \Delta\omega}\right\}$$

$$= \frac{1}{\mathrm{Re}\left[\overline{\sum_{m}^{N_s} \tilde{F}_m^* \tilde{\dot{s}}_m}^{\omega, \Delta\omega}\right]} \mathrm{Re}\left\{\overline{\sum_{m}^{N_s}\sum_{r}^{N_r} \frac{(B_{mr}^2 \tilde{\ddot{s}}_m \tilde{F}_m^* + \sum_{k\neq m}^{N_s} B_{mr}B_{kr}\tilde{\ddot{s}}_k \tilde{F}_m^*)(-i\omega)}{Z_r^*(\omega)\, Z_m^*(\omega)}}^{\omega, \Delta\omega}\right\} \tag{53}$$

Again, from integral approximation, but summing first with respect to r in a procedure entirely analogous to that for Eq. (11-1) of Lyon and Maidanik[11], the first double sum in Eq. (53) is

$$a_m = \mathrm{Re}\left\{\overline{\sum_{m}^{N_s}\sum_{r}^{N_r} \frac{-B_{mr}^2 \tilde{\ddot{s}}_m \tilde{F}_m^* i\omega}{Z_r^*(\omega)\, Z_m^*(\omega)}}^{\omega, \Delta\omega}\right\} \Big/ \mathrm{Re}\left[\overline{\sum_{m}^{N_s} \tilde{F}_m^* \tilde{\dot{s}}_m}^{\omega, \Delta\omega}\right]$$

$$= \frac{1}{2}\overline{B_{mr}^2}^{N_r(\omega)}\, n_r(\omega)\, \frac{\pi^2}{2\Delta\omega}, \qquad \tilde{\ddot{s}}_m = -i\omega\tilde{\dot{s}}_m$$

$$= \frac{\pi}{2} \cdot \frac{R_{rad}}{\Delta\omega M} \Rightarrow \frac{\pi}{2} \cdot \frac{\omega}{\Delta\omega}(\eta_{23} + \eta_{21}) \tag{54}$$

Considerable effort would be involved in determining a_k if $k \neq m$, which is

$$a_k = \mathrm{Re}\left\{\overline{\sum_{m}^{N_s}\sum_{r}^{N_r} \frac{B_{mr}B_{kr}\tilde{\ddot{s}}_k \tilde{F}_m^*(-i\omega)}{Z_r^*(\omega)\, Z_m^*(\omega)}}^{\omega, \Delta\omega}\right\} \Big/ \mathrm{Re}\left[\overline{\sum_{m}^{N_s} \tilde{F}_m^* \tilde{\dot{s}}_m}^{\omega, \Delta\omega}\right] \tag{55}$$

$$\alpha_{rad} = \sum_{k}^{N_s} \alpha_k \tag{56}$$

For $N_s \neq 0$, the minimum possible value of α_k may be α_m while the maximum possible value may be $N_s\alpha_m$. As an estimate of the correction for later discussion, we shall use

$$1 + \alpha_{rad_{AF}} \cong 1 + \left(\frac{N_s + 1}{2}\right) \alpha_m = 1 + \left(\frac{I_{2AF} + 1}{2}\right) \cdot \frac{\omega}{\Delta\omega} (\eta_{23AF} + \eta_{21AF}) \frac{\pi}{2} \tag{57}$$

Note that α_{rad_s} is negligible for other than acoustic fast modes.

Coupling Factors

The radiation coefficient R_{rad} for a flat panel was derived by Maidanik[17] with some simplifying assumptions. However, there is some ambiguity and apparent inapplicability. Some revised forms were given in Crocker and Price[12] which do not seem to be entirely consistent with Maidanik's statements, thus requiring new interpretation. Nevertheless, a detailed mathematical rederivation of Eqs. (2-39a, b, c) of Maidanik will not be performed here due to limitation of time available and may not necessarily be needed. Therefore, we apply the given forms to the present case directly.

The coincidence frequency f_c for our experiments is 23,300 Hz, which is much higher than the maximum frequency in our tests. Thus, we shall apply equations for this range $f < f_c$, i.e., Eqs. (2.39 a, b, c) of Maidanik[17]. This is based on Maidanik's statement above Eq. (2.38) that "We shall

therefore confine our attention to frequencies below the coincidence frequency."
In Maidanik's notation list, he defined k_p as panel wave length and f_p as coincidence frequency of the panel, which will be replaced by f_c.

Equation (2.39a) of Maidanik is then

$$R_{rad_{AS}} = A\rho_0 c_0 \left\{ 2\alpha^2(\lambda_a\lambda_c) G_1(f/f_c) + (P_r\lambda_c/A) G_2(f/f_c) \right\}$$

$$\text{for } k_p > k_a, \text{ i.e., } c_p < c_0 \text{ or AS modes} \qquad (58)$$

where

$$\alpha = \sqrt{f/f_c} \qquad (59)$$

$$G_1(f/f_c) = (4/\pi^4)(1 - 2\alpha^2)/\alpha(1 - \alpha^2)^{1/2}, \quad f \leq \frac{1}{2} f_c \qquad (60a)$$

$$G_1(f/f_c) = 0, \quad f \geq \frac{1}{2} f_c \qquad (60b)$$

$$c_p = \frac{\omega}{k_p}, \quad k_a = \frac{\omega}{c_0} \qquad (60c)$$

$$G_2(f/f_c) = \frac{1}{(2\pi)^2} \left\{ (1 - \alpha^2) \ln [(1 + \alpha)/(1 - \alpha)] + 2\alpha \right\} / (1 - \alpha^2)^{3/2} \qquad (61)$$

$$\lambda_c = \frac{c_0}{f_c} \qquad (62a)$$

$$\lambda_a = \frac{c_0}{f} \qquad (62b)$$

The factor $2\alpha^2$ in the first term inside the brace of Eq. (58) was first corrected by Crocker and Price[12] and confirmed by Maidanik through a private communication. The range of applicability has been modified and is consistent with all known usage in the literature, i.e., for AS modes.

In our case, the perimeter of an equivalent plate is

$$P_r = 4\pi a + 2\ell \tag{63}$$

Equation (2.39c) of Maidanik[17] is then

$$R_{rad} = A\rho_0 c_0 [1 - f/f_c]^{-1/2} = R_{rad_{AF}} \quad \text{for } k_p < k_a, \text{ i.e., i.e., } c_p > c_0 \text{ or AF modes} \tag{64a}$$

Maidanik's branching condition of $f > f_c$ is inapplicable since the square root becomes imaginary, while the modification by Crocker and Price[12] is inconsistent with the stated range $f < f_c$. As in our problem $f << f_c$, Eq. (64a) yields

$$R_{rad_{AF}} \cong A\rho_0 c_0 \quad \text{for AF modes} \tag{64b}$$

which has been used for panels and is apparently justified. Similarly, Eq. (2.39b) of Maidanik could be for $k_p = k_a$ which shows a discontinuity in radiation coefficient from AF to AS modes. In any event, this equation has not been used in practice and will not be discussed further.

As pointed out by Crocker and Price[12], Eq. (58) applies for AS modes which are edge modes, thus proportional to its effective edge. The resistance for radiation from the cylindrical shell to the exterior through AS modes is then

$$R_{2l_{AS}} = R_{rad_{AS}}^{3/4 \text{ space}} = \frac{2}{3} R_{AS}^{1/2 \text{ space}} = \frac{2}{3}\left(\frac{2\pi a}{2\pi a + 2\ell}\right) R_{rad_{AS}} \tag{65}$$

The additional idea of edge modes being inversely proportional to the relative value of the space the edge "looks into" was first introduced by Lyon[18]. It might be justifiable by an integral equation approach, as the contribution or residue of a source at the edge is directly proportional to the solid angle of the space it looks into. Thus, the local potential would be inversely proportional to this angle. This alternative approach might yield an improved result or provide a check on Maidanik's[17] result based on Lyon and Maidanik's[11] approximate formula. Similarly, the resistance for radiation from the cylindrical shell into the interior through AS modes is

$$R_{23_{AS}} = R_{rad_{AS}}^{1/4 \text{ space}} = 2R_{AS}^{1/2 \text{ space}} = 2\left(\frac{2\pi a}{2\pi a + 2\ell}\right) R_{rad_{AS}} \tag{66}$$

The AF modes, however, as discussed by Crocker and Price[12] are surface modes; therefore, they are independent of the total length of the edges and the space they look into. The radiation resistance is approximately the same for the cylinder and a rectangular plate, that is

$$R_{21_{AF}} = R_{23_{AF}} = R_{rad_{AF}} \tag{67}$$

Finally, the coupling factors as indicated by Eqs. (15), (16), and (35) are

$$\eta_{2j_s} = \frac{R_{2j_s}}{M\omega} \tag{68}$$

where j = 1, 3 and s stands for AF, AS modes, respectively. For non-radiation modes, the radiation is negligible.

Loss Factors

Viscoelastic Structural Damping

The structural damping depends on the physical mechanism of the material during loading and unloading[19]. There are viscoelastic damping and hysteresis damping, macroscopically. For an aluminum beam with simple-edge conditions, Baker, Woolam, and Young[20] have found that the hysteresis damping is negligible compared with viscoelastic damping. Their results are in agreement with experiments which account for the contribution of air damping. Thus, a similar theory will be applied in the present problem.

Based on viscoelastic theory, the effective modulus of elasticity, E_V, and Poisson's ratio, ν_V are[21]

$$E_V = \frac{3k_V\mu_V}{k_V + \frac{1}{3}\mu_V} \tag{69}$$

$$\nu_V = \frac{k_V - \frac{2}{3}\mu_V}{2\left(k + \frac{1}{3}\mu_V\right)} \tag{70}$$

The effective bulk modulus k_V is assumed to be independent of viscoelastic effects; thus

$$k_V = k \tag{71}$$

In terms of Lame constants λ and μ, the elastic modulus, Poisson's ratio, and bulk modulus are, respectively:

$$E = \frac{3k\mu}{k + \frac{1}{3}\mu}, \quad \nu_e = \frac{\lambda}{2(\lambda + \mu)}, \quad k = \lambda + \frac{2}{3}\mu = \frac{E}{3(1 - 2\nu)} \qquad (72a, b, c)$$

The viscoelastic Lame constants in terms of the Laplace transform variable s are

$$\mu_v = \frac{s^n b_n + \ldots + b_0}{2(s^m a_m + \ldots + a_0)} \qquad (73)$$

$$\lambda_v = k - \frac{2}{3}\mu_v \qquad (74)$$

For periodic motion proportional to $e^{i\omega t}$,

$$s = i\omega \qquad (75)$$

For standard linear solids, only first derivatives exist; thus

$$\mu_v = \frac{1 + i\omega(E'/E)}{1 + i\omega C'}\mu \qquad (76)$$

which becomes μ in the limit of zero frequency. From Eqs. (69), (70), (71), (72a, b), and (76), one finds

$$E_v = E\left\{\frac{1}{(1 - 2\nu_e)} \cdot \frac{1}{2(1 + \nu_e)}\left[\frac{1 + i\omega(E'/E)}{1 + i\omega C'}\right]\right\} \Bigg/ \left\{\frac{1}{3(1 - 2\nu_e)} + \frac{1}{3} \cdot \frac{1}{2(1 + \nu_e)}\left[\frac{1 + i\omega(E'/E)}{1 + i\omega C'}\right]\right\} \qquad (77)$$

$$\nu_v = \frac{1}{2}\left\{\frac{1}{3(1-2\nu_e)} - \frac{2}{3}\left[\frac{1+i\omega(E'/E)}{1+i\omega C'}\right]\frac{1}{2(1+\nu_e)}\right\} \Big/ \left\{\frac{1}{3(1-2\nu_e)} + \frac{1}{3}\left[\frac{1+i\omega(E'/E)}{1+i\omega C'}\right]\frac{1}{2(1+\nu_e)}\right\} \tag{78}$$

In general, the vibration of a viscoelastic shell can be obtained from vibration of elastic shell with simple damping term correction. However, for nearly incompressible medium $\nu_e \to \frac{1}{2}$, the limit of Eq. (78) yields $\nu_v = \frac{1}{2} = \nu_e$ as expected, and that of Eq. (77) yields

$$E_v = E\left[\frac{1+i\omega(E'/E)}{1+i\omega C'}\right] \tag{79}$$

As an approximation, we shall use actual values of ν_e for ν_v and E_v given by Eq. (79). Then, the equation for the vibration of cylindrical shell in terms of normal modes W_{mn} becomes

$$\frac{1+i\omega(E'/E)}{1+i\omega C'}\,\omega_{mn}^2 W_{mn} + \frac{\partial^2 W_{mn}}{\partial t^2} = 0 \tag{80}$$

Since $i\omega$ is equivalent to the operator $\frac{\partial}{\partial t}$, this actually means

$$\omega_{mn}^2 W_{mn} + \frac{E'}{E}\omega_{mn}^2 \frac{\partial W_{mn}}{\partial t} + \frac{\partial^2 W_{mn}}{\partial t^2} + C' \frac{\partial^3 W_{mn}}{\partial t^3} = 0 \tag{81}$$

To get an effective damping, let the solution be

$$W_{mn} = e^{(i\omega - \delta)t} \tag{82}$$

Then, the real and imaginary parts of Eq. (81) yield:

$$\omega_{mn}^2 - \alpha_0\delta - \omega^2 + \delta^2 + 3\delta C'\omega^2 - \delta^3 = 0 \tag{83a}$$

$$\alpha_0\omega - 2\delta\omega - C'\omega^2 + 3\delta^2 C'\omega = 0 \tag{83b}$$

where

$$\alpha_0 = \frac{E'}{E}\omega_{mn}^2 \tag{84}$$

For a small damping constant δ, the δ^2 term in Eqs. (83a,b) probably can be neglected, and

$$\delta \cong \frac{1}{2}\left[\alpha_0 - C'\omega^2\right] \tag{85}$$

Similarly, Eqs. (84) and (85) yield

$$\omega^2 \cong \omega_{mn}^2 - \delta^2 + 2C'\omega^2\delta \cong \omega_{mn}^2 - \delta^2 + 2C'\omega^2\delta \cong \omega_{mn}^2 + 2C'\omega^2\delta \tag{86}$$

Substituting Eqs. (82) and (86) into (85) and solving for 2δ, one finds

$$\beta_{mn} = 2\delta = \frac{\left(\frac{E'}{E} - C'\right)\omega_{mn}^2}{1 + (C')^2\,\omega^2} \tag{87}$$

which agrees with Baker-Woolam-Young's results for a beam. Finally, the logarithmic decrement is

$$\delta_{dec} = \left(\frac{2\pi\delta}{\omega}\right)_{\omega=\omega_{mn}} = \frac{\pi\Delta_1\omega_{mn}}{1 + C\omega_{mn}^2} \tag{88}$$

where

$$\Delta_1 = \frac{E'}{E} - C', \quad C = (C')^2 \tag{89}$$

Since these constants depend on thickness, known experimental values[20] are not applicable to our shell of thickness 0.02 inch. Therefore, logarithmic decrements were measured for our shell in air, results of which are shown in Figure 8. Matching of the theoretical and experimental logarithmic decrements was made at f = 200 Hz and f = 4000 Hz in order to determine Δ_1 and C as

$$\Delta_1 \cong 5.33 \times 10^{-6} \Big/ \left(\frac{\text{rad}}{\text{sec}}\right) \tag{90a}$$

$$C = 2.28 \times 10^{-7} \Big/ \left(\frac{\text{rad}}{\text{sec}}\right)^2 \tag{90b}$$

The theoretical curve of Figure 8 was then computed by using these values in Eq. (88). The above two frequencies were particularly appropriate for matching the damping data, as preliminary investigations showed no acoustic fast modes in both frequency bands, so that the air damping due to radiation is relatively insignificant at these frequencies. Further, the resulting theoretical damping allowed good general agreement with experimental results for shell response, and plausible explanations for some discrepancies to be discussed later.

Since only resonant modes in the narrow frequency band are needed in the prediction, $\omega_{mn} \cong \omega$. Thus, the effective damping

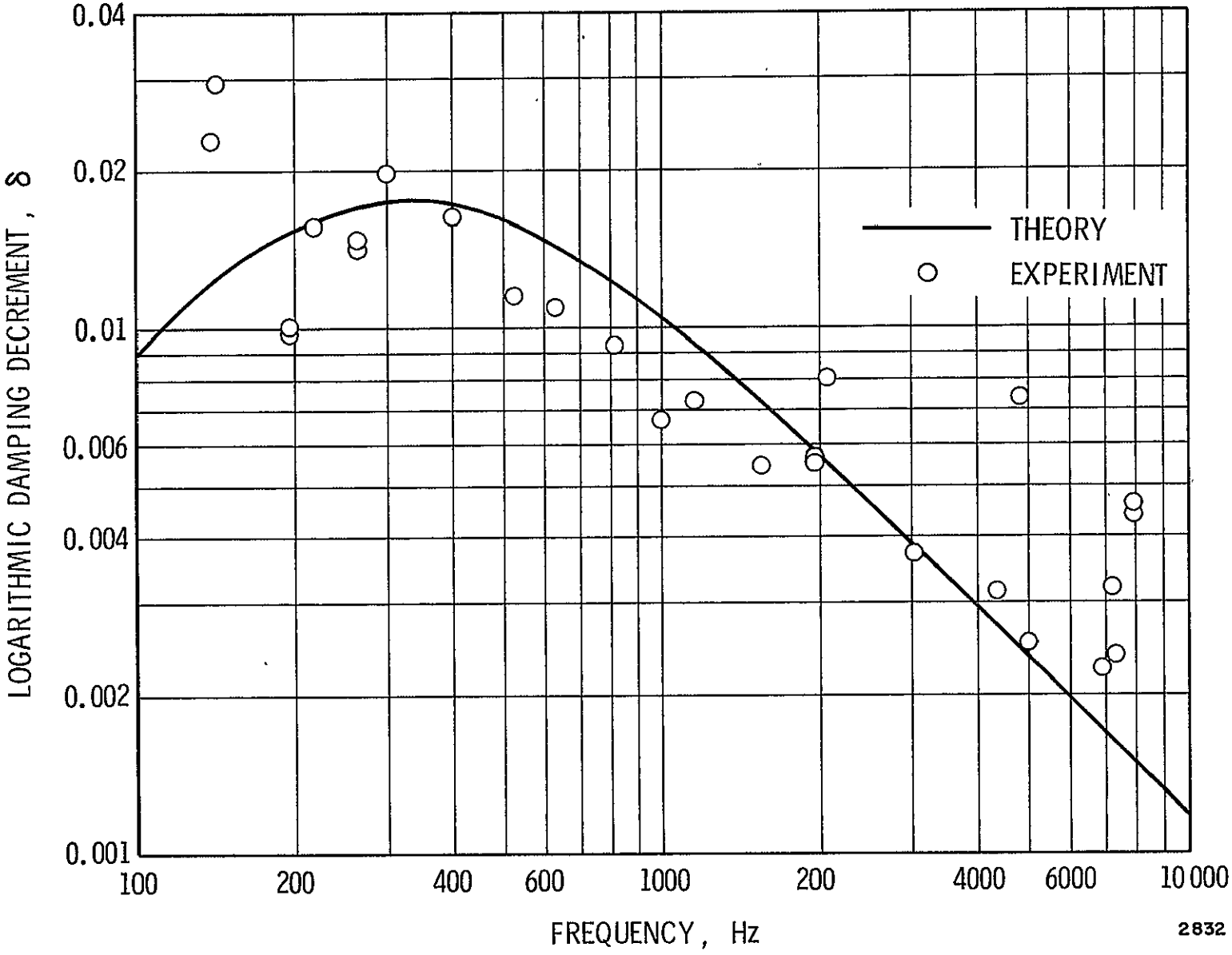

Figure 8. Damping Decrement For Cylindrical Shell

coefficient for all modes in the frequency band centered at ω is approximately

$$\beta_s \equiv \beta_2 = 2\delta = \frac{\Delta_I \omega^2}{1 + C\omega^2} = \frac{\left(\frac{E'}{E} - C'\right)\omega^2}{1 + (C')^2\omega^2} \tag{91}$$

When $C' = 0$, Eq. (81) reduces to second order and Eq. (91) yields $(E'/E)\omega_{mn}^2$, which is the correct damping coefficient. Comparing Eqs. (7) and (21), the loss factor η_s is then

$$\eta_s = \eta_2 = \beta_s/\omega \tag{92}$$

which is non-dimensional, as it should be.

Air Damping

When there is negligible dispersion of sound due to wind and turbulence, there are two properties of the medium causing combined attenuation of a wave propagating in a "free space." The first is the molecular absorption and dispersion in polyatomic gases involving exchange of translational and vibrational energy between colliding molecules, and the second is dissipation due to viscosity and heat conduction in the medium.[22] The attenuation due to the first is α_M and that due to the second is α_C, which is the sum of α_η, due to viscosity, and α_T, due to thermal, conductivity. The total theoretical attenuation is

$$\alpha_A = \alpha_M + \alpha_C \tag{93}$$

Graphs are available to determine α_M and α_C directly and indirectly (see Figures 3d-1 and 3d-2 of Reference 22). However, some difficulty was encountered, and the resultant damping appeared to be of wrong magnitude to check the measured pressure spectral density at 200 Hz. Fortunately, an empirical equation which describes the measured values of Knudsen and Harris with good accuracy† for relative humidities above 30 percent and at temperatures near 20°C is also given, and is valid for our experimental conditions. This equation states

$$\alpha_A = \left(\frac{f}{1000}\right)^{3/2} \frac{0.085}{20 + \phi_T} \qquad \text{ft}^{-1} \tag{94}$$

where f is the frequency in Hz and

$$\phi_T = \phi_{20}(1 + 0.067)\,\Delta T \text{ (non-dimensional)} \tag{95}$$

ϕ_{20} is the relative humidity at 20°C and ΔT the temperature difference from 20°C. Since Eq. (94) is insensitive to small differences in temperature and humidity, we have taken $\Delta T \cong 0$ and $\phi_{20} = 0.5$; thus, the denominator is approximately 20.5.

The attenuation factor is given as $e^{-\alpha_A x}$; hence, a one-dimensional theory is used to correlate the damping coefficient, i.e.,

$$\frac{1}{c_0^2}\left(\frac{\partial^2 \beta}{\partial t^2} + \beta_a \frac{\partial p}{\partial t} - c_0^2 \frac{\partial^2 p}{\partial x^2}\right) = \frac{1}{c_0^2} \cdot \frac{\partial^2 p}{\partial t^2} + \frac{\beta_a}{c_0^2} \cdot \frac{\partial p}{\partial t} - \frac{\partial^2 p}{\partial x^2} = 0 \tag{96}$$

†This is true if the unit is 1/ft instead of dB/ft.

The attenuated solution for small damping is

$$p = p_0 e^{-i\sqrt{\left(\frac{\omega}{c_0}\right)^2 - i\left(\frac{\beta_a}{c_0^2}\right)\omega}\, x + i\omega t}$$

$$\cong p_0 e^{i\omega t - i\frac{\omega}{c_0} x - \frac{1}{2}\cdot\frac{\beta_a}{c_0} x} \tag{97}$$

Therefore

$$\beta_a = 2c_0\alpha_A \tag{98}$$

Analogous to the relation between Eqs. (91) and (92), the loss factor in air is

$$\eta_3 = \eta_a = \beta_a/\omega = 2\alpha_A\, c_0/\omega \tag{99a}$$

where

$$\alpha_A \cong \left(\frac{f}{1000\ \text{Hz}}\right)^{3/2} \frac{0.085}{20.5} \tag{99b}$$

Based on Figure (3d-3) of Reference 22, the frequency range for the validity of Eq. (94) and thus of Eq. (99b), seems to be 10,000 Hz, beyond which the accuracy of approximation would be unknown. In our tests, the frequency of interest was below this value, and the use of Eq. (94) or Eq. (99b) seems to be well justified.

RESULTS AND DISCUSSION

Comparison of Theory and Experiment

In effect, results for structural damping have already been presented in Figure 8. This, of course, was desirable for describing the method utilized to determine material constants. However, at this point, it is appropriate to discuss some of its limitations. As can be seen in Figure 8, considerable scatter resulted in the experimental data. Such scatter occurs with either method used to determine damping. With the free-decay method, scatter results from nonuniformity of decay curves which is caused by the beating of modes in proximity to each other. On the other hand, with the half-bandwidth technique, an erroneous damping usually results from the spatial shifting about of modal patterns, as well as coupling between nearby modes. With a fixed point for response observation, spatial shifts of modal pattern with frequency have a strong influence on the damping estimate. A much better determination of structural damping in cylinders is badly needed for the prediction of response to not only random, but to all forms of forced excitation.

The cylinder and interior air cavity responses, parameters for which are given in Figures 9 through 11, are the central results for this entire study. Several kinds of data are shown in each figure. Part of the results will be discussed in this section, while the rest will be discussed along with additional supporting data in the next section. In general, details of theoretical computations will first be presented, and then their results will be compared with experimental data.

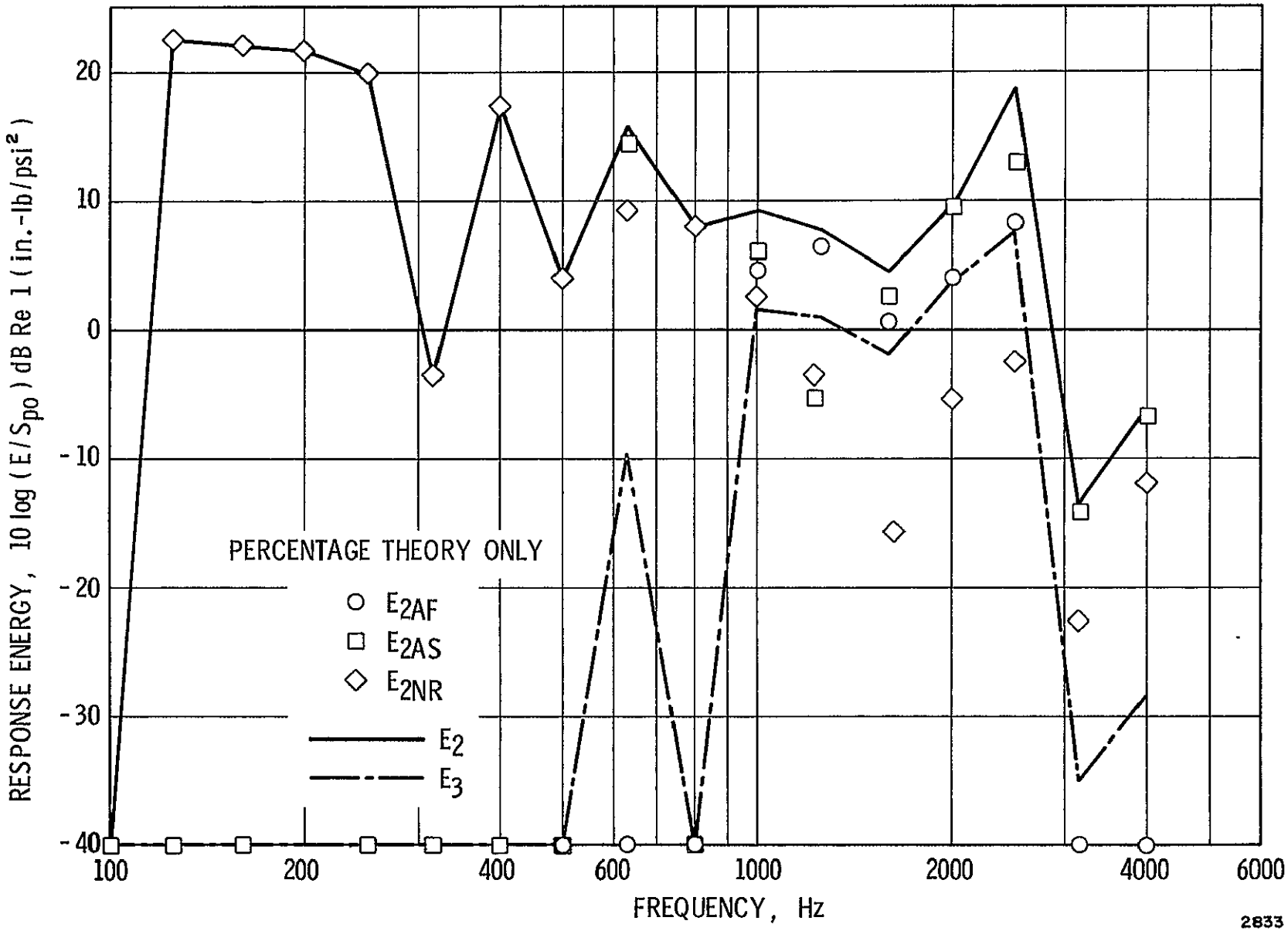

Figure 9. Energy Distribution For System

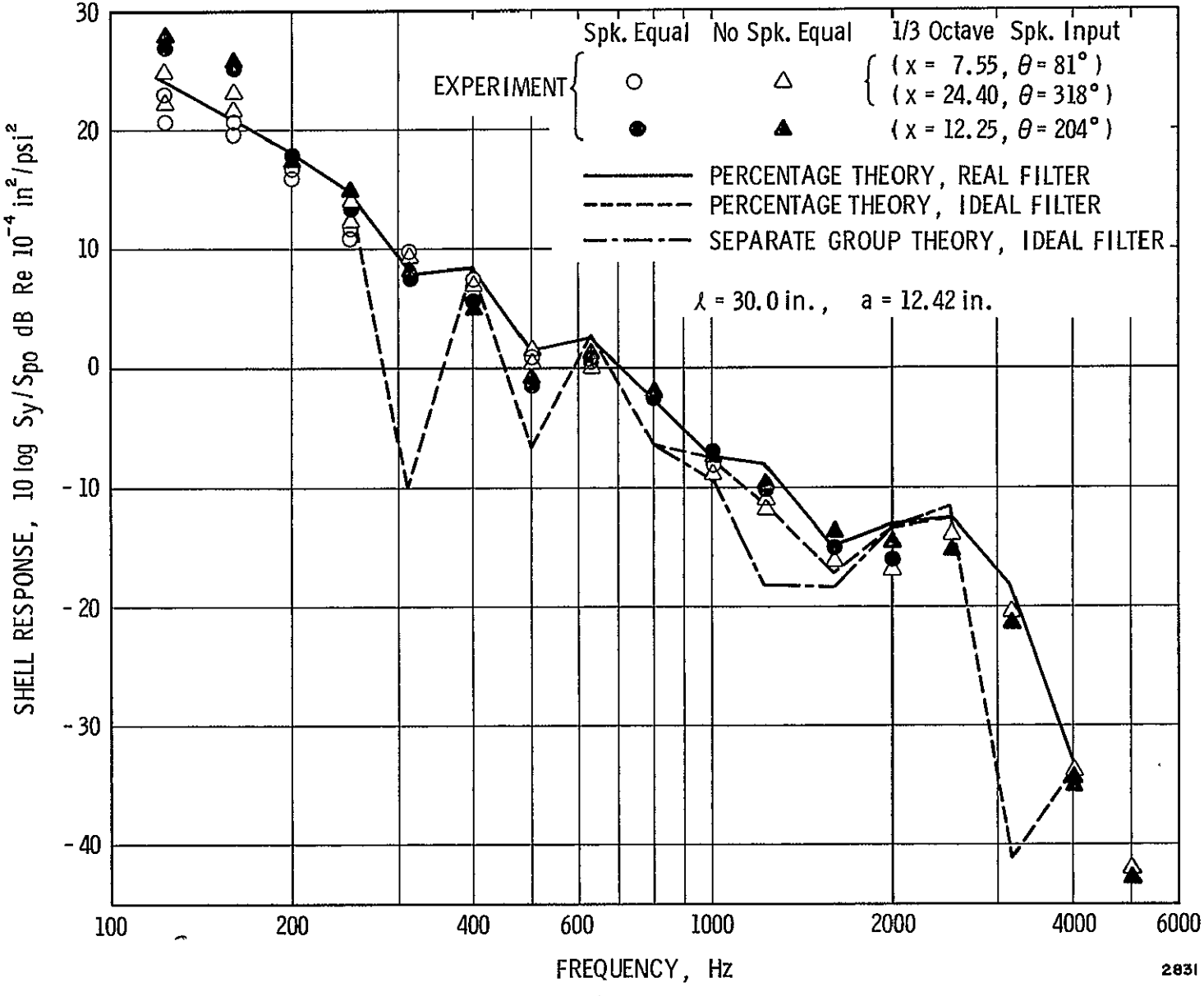

Figure 10. Shell Response Ratio

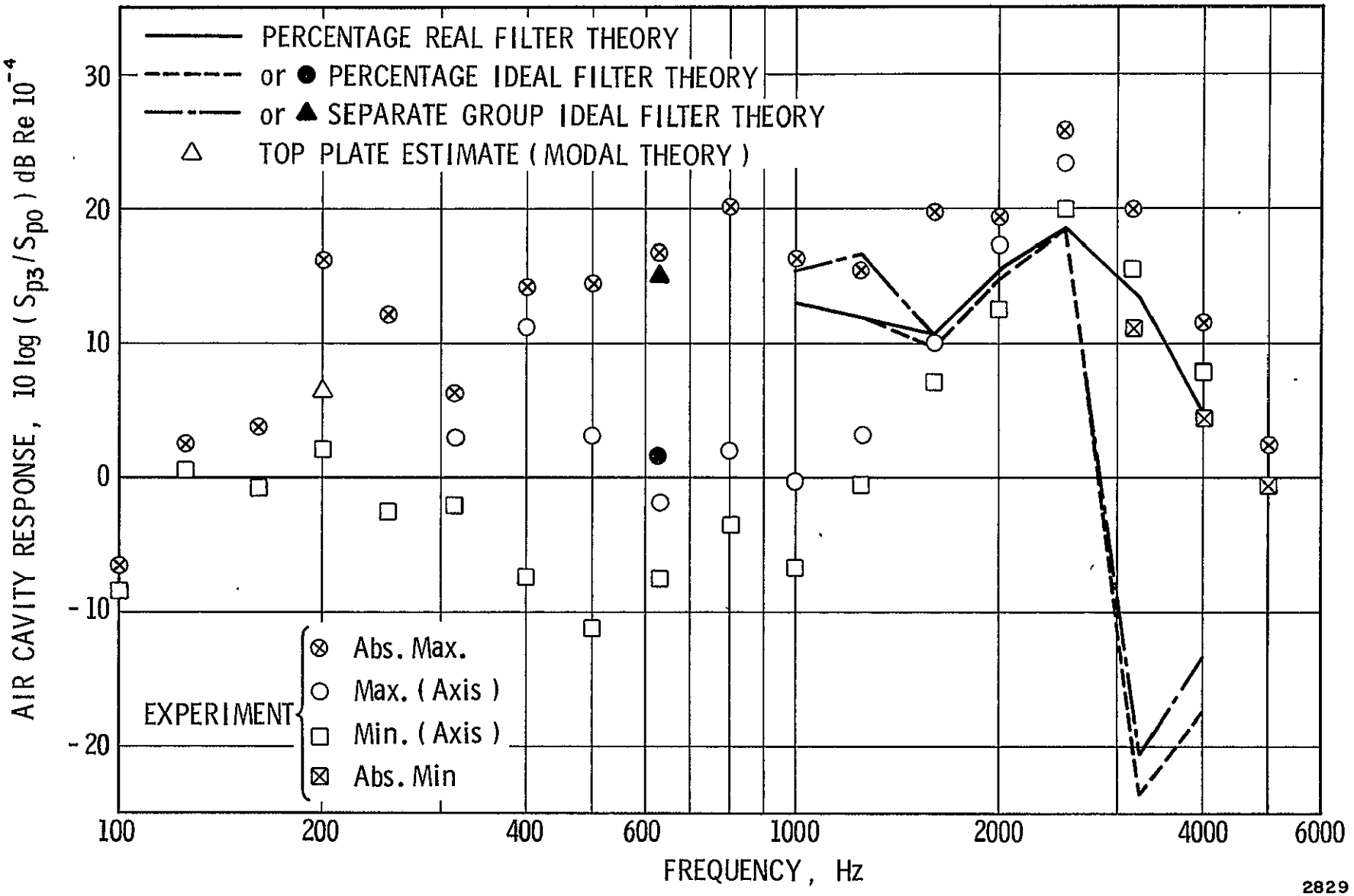

Figure 11. Air Cavity Response Ratio

Figure 9 presents the system energy distribution obtained by means of the percentage method only, and is useful for studying some details of the statistical energy method. These results are purely theoretical and include the assumption of an ideal 1/3-octave filter. On the other hand, response results for cylinder displacement and interior air cavity can more readily be compared with measured values. Correlations for these parameters are shown in Figures 10 and 11. In these figures, the dashed theoretical curves (for both separate group and percentage methods) are based on the assumption of an ideal rectangular 1/3-octave filter, the solid lines represent theoretical curves (for percentage method only) which have been corrected for the real filter characteristic, while multiple experimental values are given at the various frequencies. In Figure 10, measurements are shown for three different observation points for broadband equalized excitation through 2500 Hz, and 1/3-octave excitation throughout the entire frequency range. In Figure 11, the pressure measurements represent maximum and minimum values observed along the centerline of the cylinder, as well as the absolute maximum or minimum value measured anywhere in the tank, for 1/3-octave excitation in the respective frequency band.

For convenient reference, the governing equations, on which the theoretical calculations are based, are listed in Table IV, along with their coefficients and the determining equations for these coefficients. The four basic Eqs. (15) through (18) for the percentage method must be solved simultaneously to determine the four unknown responses E_{2AF}, E_{2AS}, E_{2NR}, and E_3 in terms of the reference excitation power spectral density S_{p_0}. The

TABLE IV. EQUATION REFERENCE FOR CALCULATIONS

Unknown Variables	Determined By Equations
E_{2AF}, E_{2AS}, E_{2NR}, E_3	Percentage Method: (15), (16), (17), (18) Separate Group Method: (8), (9), (10), (11)
Coefficient	
η_2	(92), (91), (90a), (90b)
η_3	(99a), (98), (99b)
η_{23AF}	(68), (67), (64b)
η_{21AF}	(68), (67), (64a)
η_{23AS}	(68), (66), (58)
η_{21AS}	(68), (65), (58)
E_2	(19)
n_2	(20)
n_3	(24)
n_{2AF}	(23)
n_{2AS}	(23)
n_{2NR}	(23)
P_{2AF}^{IN}	(44), (45b), (50), (51a), (51b), (51c), (52a), (52b), Fig. 6, and (57), (68), (67), (64a)
P_{2AS}^{IN}	
P_{2NR}^{IN}	

results are then plotted as in Figure 9. Subsequent use of Eqs. (27) and (29) then allows a determination of the response ratios as they appear in Figures 10 and 11. Similar calculations are performed for the separate group method, except that Eqs. (8) through (11) are used as the governing equations instead.

A matrix inversion scheme on a digital computer was used for the above solution. Several comments must be made to clarify some of the details of this procedure. Calculation of input power coefficients requires the evaluation of joint acceptance functions by means of Eqs. (51a) and (52a). A numerical integration scheme employing a mesh size of 0.4 in. was used for this purpose. Further, identification of specific wave numbers, m and n, for each of the modes in the respective 1/3-octave bands also had to be included. This identification, along with a mode count, was done from the modal diagram in Figure 6. All computations then included several parameters which were based on some form of 1/3-octave average value, which was usually a value determined at the band center frequency. These were:

(1) Spatial distribution of excitation pressure

(2) Viscoelastic structural damping

(3) Air damping coefficients

(4) Radiation coupling factors

(5) Modal density of interior air cavity.

It is interesting to look at the results of Figure 9 with one major assumption of the percentage method in mind. In particular, the respective energies are combined with the modal densities to provide the tabulated energy densities per mode given in Table V. It is apparent that the assumptions

TABLE V. ENERGY DENSITY DISTRIBUTION

f, Hz	E_{2AF}/I_{2AF}	E_{2AS}/I_{2AS}	E_{2NR}/I_{2NR}	E_2/I_2	E_3/N_3
125	--	--	90.5	90.5	0
160	--	--	54.0	54.0	0
200	--	--	40.9	40.9	0
250	--	--	12.2	12.2	0
315	--	--	5.29×10^{-2}	5.29×10^{-2}	0
400	--	--	3.95	3.95	0
500	--	--	0.1192	0.1192	0
630	--	28.3	0.286	1.22	2.25×10^{-2}
800	--	--	0.138	0.138	0
1000	2.92	1.96	0.297	0.1225	8.04×10^{-2}
1250	2.15	0.1475	4.76×10^{-3}	6.06×10^{-2}	3.35×10^{-2}
1600	0.229	0.1813	1.955×10^{-4}	1.820×10^{-2}	8.26×10^{-3}
2000	0.281	0.296	1.812×10^{-2}	3.77×10^{-2}	1.635×10^{-2}
2500	0.2156	0.1111	2.46×10^{-3}	6.03×10^{-2}	1.890×10^{-2}
3150	--	2.35×10^{-4}	2.56×10^{-5}	1.023×10^{-4}	5.41×10^{-7}
4000	--	3.30×10^{-3}	3.28×10^{-4}	6.55×10^{-3}	1.39×10^{-6}
5000	--	--	--	--	--

of Eq. (12) are not very well satisfied by the final results. Nevertheless, as will be shown hereafter, the overall comparison of theoretical and experimental results for the percentage method is still quite good, and is better than that for the separate group method. This apparent contradiction simply emphasizes the dire need of further study in the application of the statistical energy method.

It must be borne in mind that the theoretical results represent space-averaged values. Measured results in Figure 10, which are taken at three rather arbitrarily selected points on the cylinder, indicate that the shell displacement response becomes reasonably uniform in space only for frequencies above 300 Hz. This, then, is the most practical frequency region where use of the statistical energy method becomes appropriate for the cylinder. That is, the actual response values at any point on the tank do not deviate appreciably from the average values, so that predicted values are of practical use. On the other hand, uniformity of air pressure in the three-dimensional interior air space never approaches that experienced by the cylinder, and only settles down to about a 6-dB spread above 2000 Hz. It appeared in this case that a measurement of maximum and minimum pressures was more useful than some average value since such an extreme spread is experienced throughout most of the frequency range. Consequently, theoretical values which represent a spacewise average should fall within the spread at all points. This does not occur near 2500 Hz. Thus, each part of the cylinder and air system independently reaches a state of relatively uniform spatial response, which corresponds to a diffuse sound field. This result is probably

influenced to some extent by the non-diffuse spatial distribution of the excitation.

The results from the separate group and percentage method (both based on an ideal filter) can readily be compared in Figures 10 and 11. For the shell response, the two methods give identical results except between about 630 and 2500 Hz. This is to be expected since no radiation occurs outside this range. However, within this range, the percentage method can be seen to provide a better comparison with experimental results. Similar behavior is apparent in the interior pressure response. Except for the single point at 630 Hz, the interior air pressure should be negligible below 1000 Hz since only non-radiating modes occur below this frequency. However, significant pressures with wide scatter obviously do occur. An attempt at explaining these observed pressures by means of so-called mass laws proved to be futile. Therefore, additional investigations were performed to try to explain this discrepancy, as well as the very obvious discrepancies between measured values and those predicted by means of theory based on the assumption of an ideal, rectangular 1/3-octave filter. The results are given in the next section.

Supporting Results

In order to provide a more detailed idea of the frequency variations in both shell displacement and interior air pressure, more resolved spectra were measured. The results appear in Figures 12 and 13, shown on a relative scale. These data are useful to provide a better idea of the respective shell and air modal densities. With the apparently wide variations in parts of the frequency range, it becomes obvious that measurements with real 1/3-octave

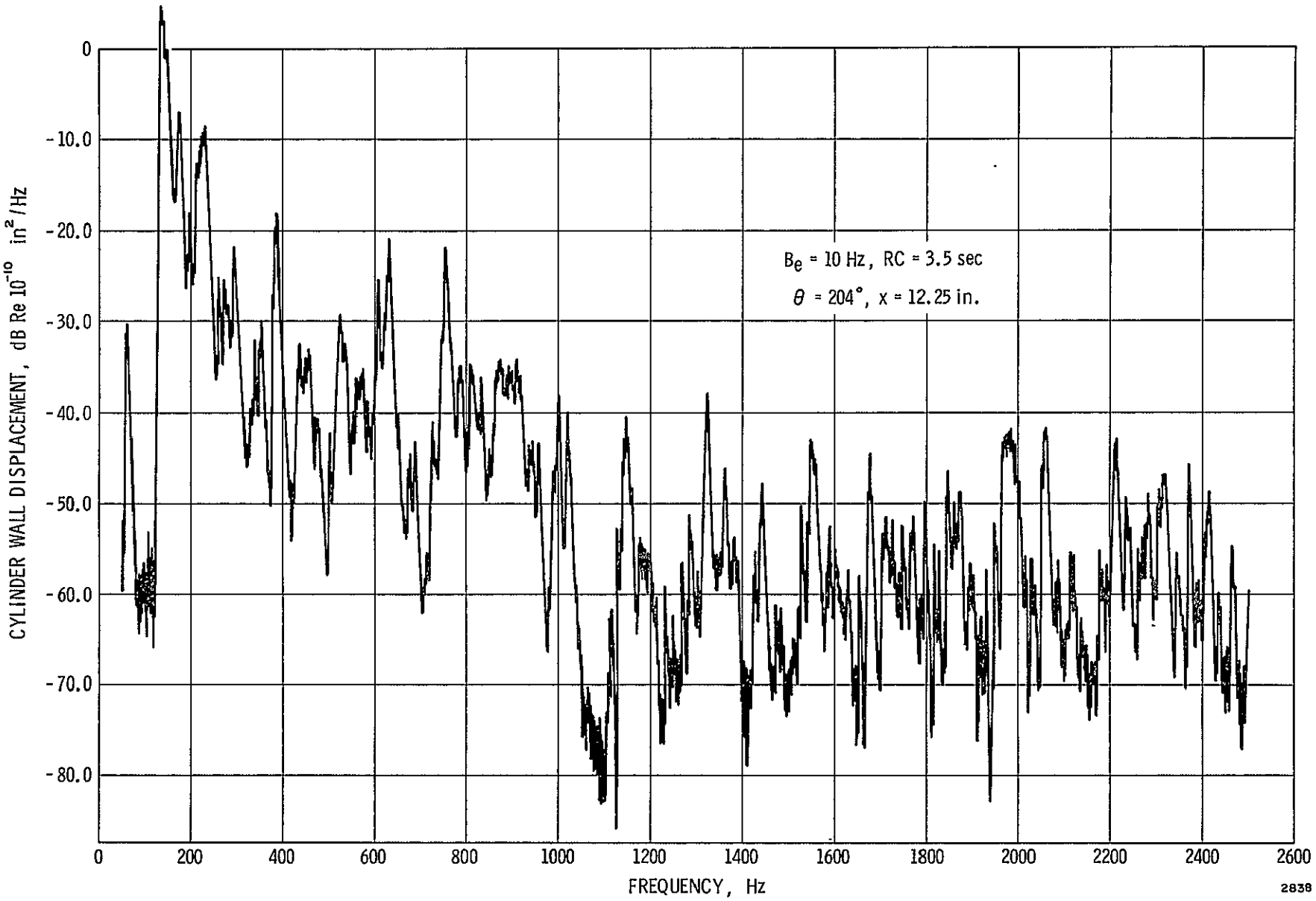

Figure 12. Highly Resolved Shell Response

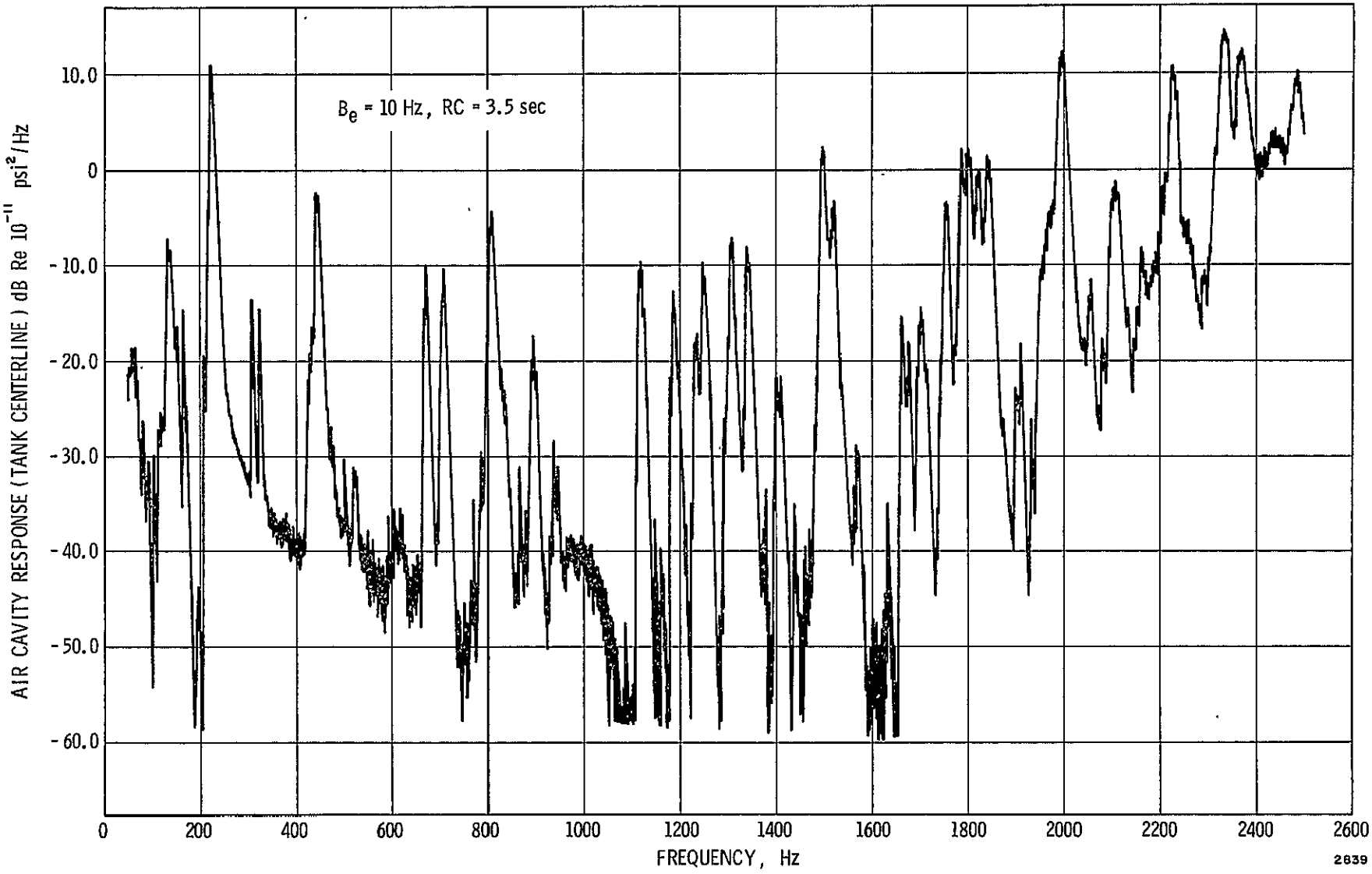

Figure 13. Highly Resolved Air Cavity Response

filters that have some finite roll-off can be in error. Further, when the excitation is filtered through such a device, low-level noise in an adjacent band can often cause a greater response than that in a particular band under concern, because of the non-flatness of the acoustical speaker. In order to allow for the non-ideal filter characteristic, a filter factor a_F and a speaker factor a_{SP} will now be derived.

The effective input is obtained from a noise generator passing the actual filter and speaker. Thus, there is additional power outside the 1/3-octave band. It is seen from Eq. (44) that P_I^{IN} is proportional to the total joint acceptance and the integrand of the joint acceptance is implicity related to $\langle p(\underline{x}', t)\, p(\underline{x}'', t)\rangle$ which, in turn, is related to p_{NG} from the noise generator. We have, in general, analogous to Eq. (40a)

$$\langle p(\underline{x}', t)p(\underline{x}'', t)\rangle = \frac{1}{T}\int_0^T p(\underline{x}', t)p(\underline{x}'', t)\, dt$$

$$= \frac{1}{2\pi T}\int_{-\infty}^{\infty} \tilde{p}^*(\omega, \underline{x}')\tilde{p}(\omega, \underline{x}'')\, d\omega$$

$$= \frac{1}{2\pi T}\int_{-\infty}^{\infty} a_F(\omega, \omega_0)\, \tilde{p}_{NG}(\omega, \underline{x}')\tilde{p}_{NG}(\omega, \underline{x}'')\, d\omega \qquad (100)$$

Therefore, the effective $\tilde{p}(\omega, \underline{x})$ is $a_F^{1/2}(\omega, \omega_0)\tilde{p}_{NG}(\omega, \underline{x})$. Analogous to Eqs. (44) (46a), and (49), we now have

$$P_I^{IN} = \frac{M}{2\pi} \cdot \frac{2}{T}\, \mathrm{Re} \sum_b \sum_{m_b} \frac{\overline{\tilde{F}_{m_b}\tilde{F}_{m_b}(-i\omega)}^{\omega,\infty}}{Z^*_{m_0}(\omega)} \qquad (101a)$$

$$\cong \frac{\pi}{2M_m} \sum_b \sum_{m_b}^{N_{b_s}} \int_{A'} \int_{A''} a_F(\omega_{m_b}, \omega_0)[k_R(\underline{x}', \omega_b; \Delta\omega_b)k_R(\underline{x}'', \omega_b; \Delta\omega_b)$$

$$+ k_I(\underline{x}', \omega_b; \Delta\omega_b)k_I(\underline{x}'', \omega_b; \Delta\omega_b)] S_{p_0}(\omega_b, \omega_0)\Delta\omega_b$$

$$\cdot \phi_m(\underline{x}')\phi_m(\underline{x}'') \, d\underline{x}' \, d\underline{x}'' \qquad (101b)$$

$$= \frac{\pi}{2M_m} \sum_b \sum_{m_b}^{N_{b_s}} a_F(\omega_{m_b}, \omega_0)a_{SP}(\omega_b, \omega_0)S_{p_0}(\omega)\Delta\omega[I_{m_b}^2 + J_{m_b}^2] \qquad (101c)$$

$$\cong \frac{\pi}{2M_m} \sum_b \left\{a_F(\omega_b, \omega_0)\, a_{SP}(\omega_b, \omega_0) \sum_{m_b}^{N_{b_s}} [I_{m_b}^2 + J_{m_b}^2]\right\} S_{p_0}(\omega)\Delta\omega \qquad (101d)$$

where

$$a_{SP}(\omega_b, \omega_0) = \frac{S_{p_0}(\omega_b, \omega_0)\Delta\omega_b}{S_{p_0}(\omega_0)\Delta\omega} = \frac{r_{SP}^{O/I}(\omega_b, \Delta\omega_b)}{r_{SP}^{O/I}(\omega_0, \Delta\omega)} \qquad (102)$$

Subscript b is for bandwidth number b, and the $r_{SP}^{O/I}$ are given in Appendix B. It is, in our case, sufficient to include the upper and lower neighboring band + and -. However, the average damping associated with ω_{m_b} in bandwidth b takes the value at ω_b. Therefore, it is more accurate to separate the equations for +, 0, and - bands and calculate the corresponding mean square shell response

$$\langle y^2 \rangle \cong \int_0^\infty S_y(\omega)\, d\omega \cong S_y(\omega_0, \omega_0)\Delta\omega + a_F(\omega_+, \omega_0)S_y(\omega_+, \omega_+)\Delta\omega_+$$

$$+ a_F(\omega_-, \omega_0)S_y(\omega_-, \omega_-)\Delta\omega_- \qquad (103)$$

$$\frac{\langle y^2\rangle}{\langle p_0^2\rangle} \cong \frac{\langle y^2\rangle}{S_{p_0}(\omega)\Delta\omega} = \frac{S_y(\omega)}{S_{p_0}(\omega)} + a_F(\omega_+, \omega_0)a_{SP}(\omega_+, \omega_0)\frac{S_y(\omega_+)}{S_{p_0}(\omega_+)}$$

$$+ a_F(\omega_-, \omega_0)a_{SP}(\omega_-, \omega_0)\frac{S_y(\omega_-)}{S_{p_0}(\omega_-)} \qquad (104)$$

which is the $S_y(\omega)/S_{p_0}(\omega)$ using a real filter with factor a_F and speaker with factor a_{SP}. For 1/3-octave filters utilized in the present study, $a_F(\omega_\pm, 0) \cong 0.16$. Eq. (104) then yields the solid line shown in Figure 10 which represents a corrected percentage method, and supports the reliability of measured data, as well as the applicability of the theory. A similar correction was applied in Figure 11. Additional measurements showed that the significant interior pressure response below 1000 Hz was being excited principally by motion of the top plate. Acceleration distribution of the top plate at various frequencies is shown in Figure 14. The plate apparently is excited by off-resonance longitudinal motion of the cylinder in its symmetric modes. Further, measurements also indicated that the pressure response was axisymmetric throughout the low range, which tended to confirm its excitation by the top plate since axisymmetric cylinder modes occurred in this frequency range. Some approximations will now be given to confirm further this behavior.

For a flat top plate moving with a constant or average amplitude W_{av}, the solution for its j^{th} axisymmetric mode is

$$\tilde{p} = \frac{-\rho_0\omega^2 a \cos\left[\sqrt{(1-ig_3)(\omega a/c_0)^2 - \lambda_j^2}\, x/a\right]}{\sqrt{(1-ig_3)(\omega a/c_0)^2 - \lambda_j^2}\sin\left[\sqrt{(1-ig_3)(\omega a/c_0)^2 - \lambda_j^2}\, \ell/a\right]} J_0(\lambda_j r)\tilde{W}_0 \qquad (105)$$

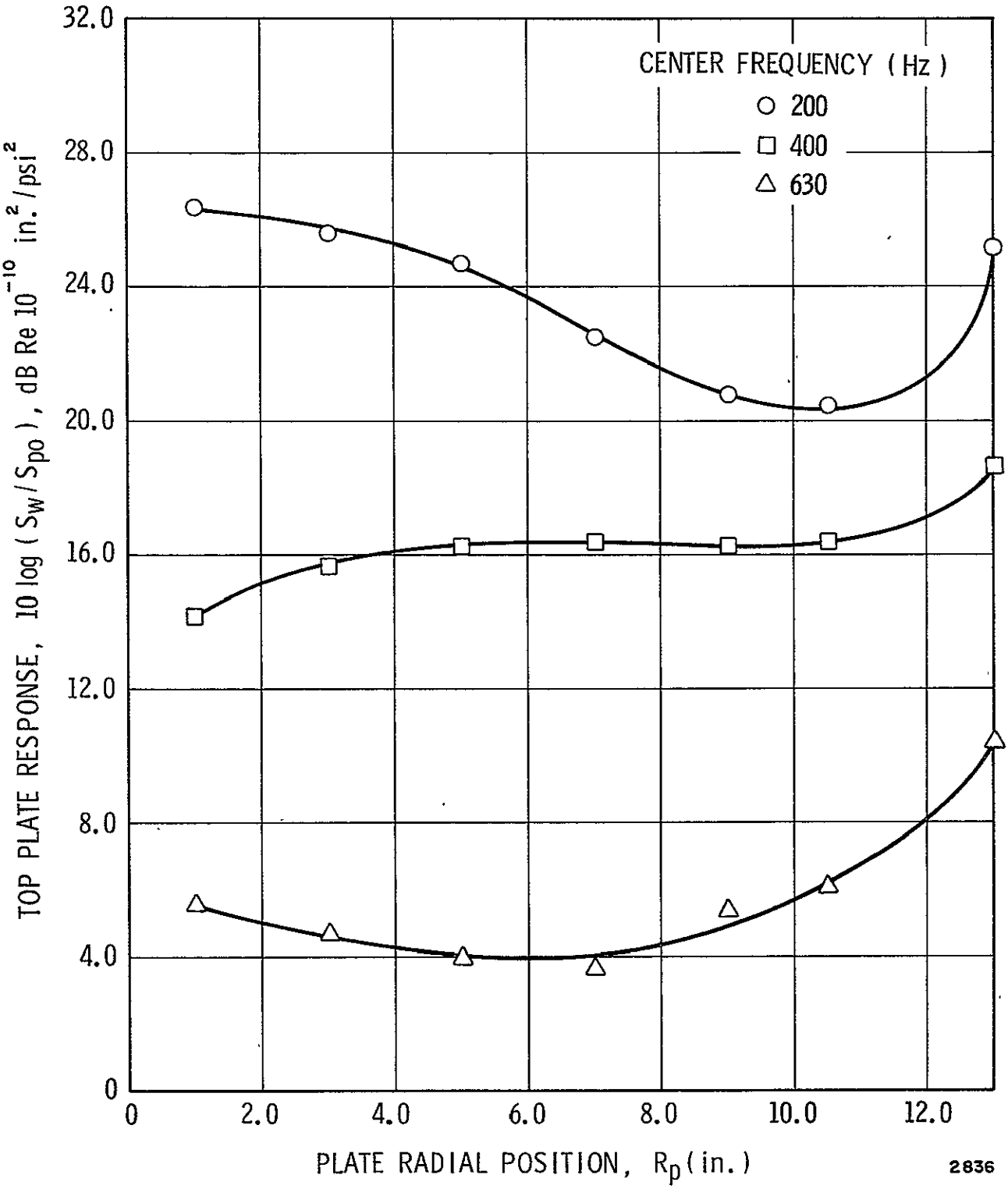

Figure 14a. Top Plate Response Ratio (200 Hz to 630 Hz)

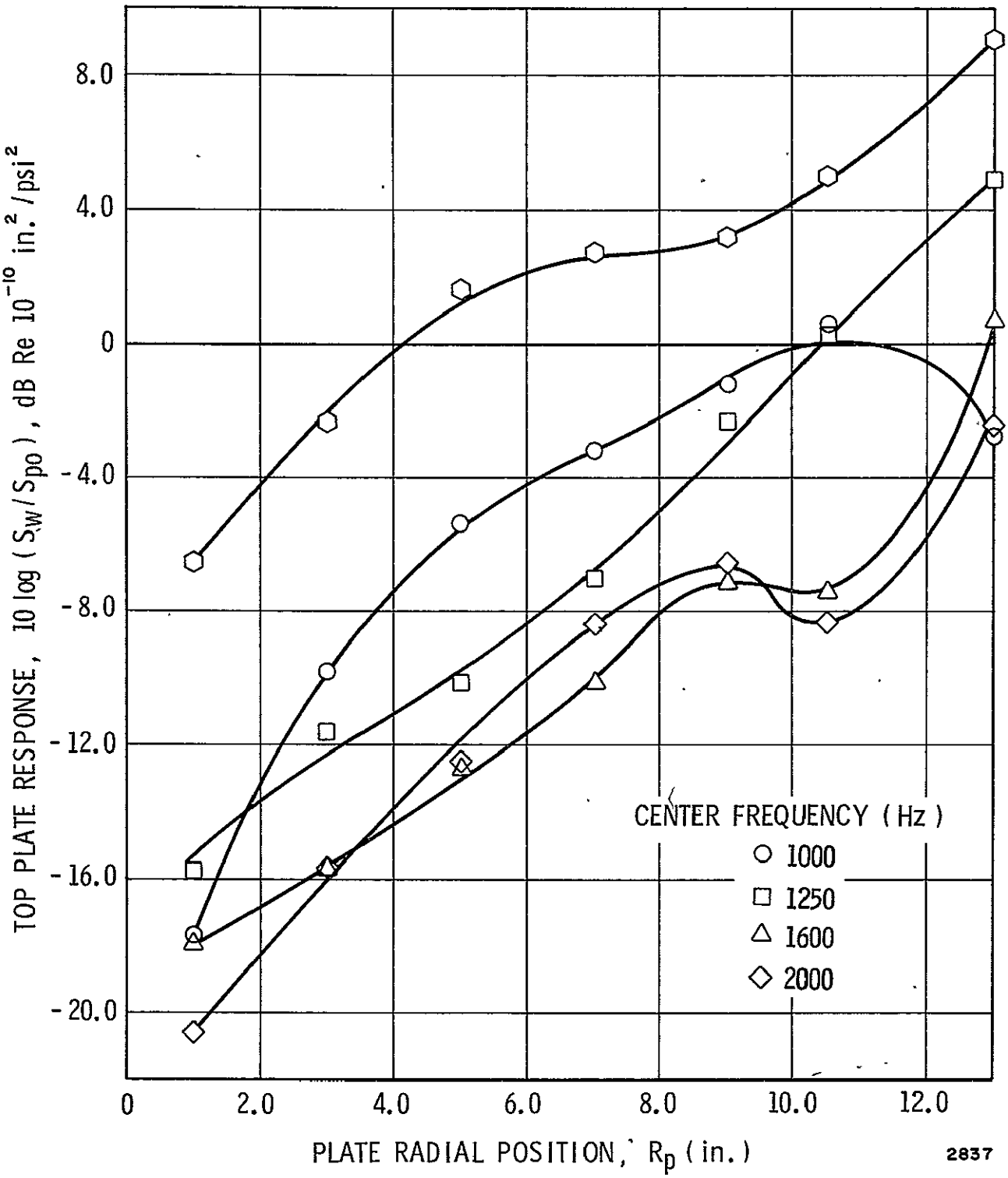

Figure 14b. Top Plate Response Ratio (1000 Hz to 2000 Hz

where λ_j is the j^{th} root of $J_1(\lambda) = 0$. Replace $J_0(\lambda_j r)\tilde{W}_0$ by $\tilde{W}_{av}$ for $j = 0$, $\lambda_j = 0$. By averaging over the frequency band, the contribution of each mode at the center of the top is

$$S_{p_{3_{mx}}} \cong \frac{\rho_0 \omega^2 c_0^2 (2\pi)}{(\ell/a)^2 g_3 (\omega_c^* \Delta\omega^*)} \left\{ \begin{matrix} S_{W_0} \\ S_{W_{av}} \end{matrix} \right\} \text{ for } \left\{ \begin{matrix} j \neq 0 \\ j = 0 \end{matrix} \right. \text{, respectively} \qquad (106a, b)$$

where

$$\omega_c^* = \frac{\omega a}{c_0}, \quad \Delta\omega^* = \frac{a}{c_0}\Delta\omega \qquad (106c, d)$$

If we assume $\tilde{W}(r, \omega)$ is proportional to $\sqrt{S_W}$, we can then calculate $S_{W_{av}}$ from S_W as given in Figure 14, and by taking into account the circular domain of the top plate, we find, for example, at 200 Hz, with $g_3 = \eta_3 = 6.49 \times 10^{-4}$, that $S_{W_{av}}/S_{p_0} = 2.114 \times 10^{-4}$. Further, in this range, there is only one resonant mode with $\lambda_j = 0$, the natural frequency of which is less than ω_c^*. Therefore, we have

$$\frac{S_{p_{3mx}}}{S_{p_0}} \cong 4.64 \times 10^{-4} = 6.7 \text{ dB Re } 10^{-4} \qquad (107)$$

This value seems to agree reasonably well with measured data (Figure 11 at 200 Hz), although it is not exactly the maximum value.

As frequency increases, more plate modes will appear which could excite $\lambda_j \neq 0$ modes. Strictly speaking, coupling coefficients should be calculated which become increasingly more complex at higher frequencies. Due to the rapid decrease in plate spectral density, an estimated S_{p_3} of the order of 10^{-8} at 4000 Hz, which is much too low. This estimate was

determined by using $\overline{S_W(r, \omega)}^r$ for S_{W_0} in Eq. (106a) to calculate $S_{p_{3_{mx}}}$ for each mode, and then multiplying by an estimated number of fifty axisymmetric modes. However, using the actual filter factors, the results at 3150 and 4000 are in reasonably good agreement with measured data.

We now consider the possibility of the rectangular room approximation as a possible source of error in the predicted values. At center frequencies of 1000, 1250, 1600, 2000, and 2500 Hz, the value of n_{2AS}/n_{2AF} is 2, 1, 2, 3.77, and 5.48, respectively, while no AF mode is present in other bands in our present range of interest. Since η_{AF} is much greater than η_{AS} (e.g., η_{AS}/η_{AF} is near the order of 0.002 in some cases), the effective radiation coefficient when $I_{2AF} \neq 0$ is approximately[6]

$$\eta_{23} \cong \frac{n_{2AF}}{n_2} \eta_{23AF} = \frac{n_{2AF}}{n_2} \eta_{AF} \tag{108}$$

For the above frequencies, Eq. (108) yields

$$E_3 = \frac{\omega \eta_{AF} E_2}{\omega \eta_3 + \omega \eta_{AF} \frac{n_2}{n_3}} = \frac{\omega \eta_{AF} E_2}{\omega \eta_3 + \omega \eta_{AF} \frac{I_2}{N_3}} \tag{109}$$

Since η_{AF}, η_3, I_2 are probably more reliable and E_2 yields correct shell response density, the doubtful quantity would be N_3 based on the number of modes present in the band in an equivalent rectangular room of the same volume. If the percentage method or the radiative power flow term is correct, the correct value of N_3 should give a good value of E_3, and the correction factor on E_3 and thus on S_{p_3} is:

$$a_{N_3} = \frac{\omega\eta_3 + \omega\eta_{AF}\frac{I_2}{N_3}}{\omega\eta_3 + \omega\eta_{AF}\frac{I_2}{I_3}} \tag{110}$$

where $N_3 = n_3(\omega)\Delta\omega$ and I_3 is the accurate number of modes in the band. With roots of $J'_n(\lambda_{nj}) = 0$ available in Reference 23 for $n \rightarrow m = 0$ to 8 and $j \rightarrow n = 1$ to 5, it is possible to find the exact value of I_3 at 1000, 1250, and 1600 Hz. For these frequencies,

$$I_3 = 13,\ 24,\ 56, \text{ respectively} \tag{111a}$$

$$N_3 = 17.9,\ 36.5,\ 75.8, \text{ respectively} \tag{111b}$$

However, with these values used in (110), the correction factor was less than 1 dB and insignificant. At 2000 and 2500 Hz, the effect is probably also small. Thus, the rectangular room estimate for interior air modal density appears to be a good approximation.

It next appeared reasonable to question the validity of the radiation coefficients as used in the present "percentage" formulation of the statistical energy method. It may be that the reverberation effect in the cross-coupling term is given in Eq. (36) may be inadequate for this purpose. As a check on this possible source of error, we return to Eqs. (30) and (31). Summing Eq. (30) with respect to m with weight $M/\Delta\omega$ yields

$$\frac{M}{\Delta\omega}\sum_m \beta_m\langle\dot{s}_m^2\rangle + \frac{M}{\Delta\omega}\sum_m\left[\sum_r g_{mr}(\omega_r, \omega_m)(\theta'_m - \theta'_r)\right]$$

$$= \frac{M}{\Delta\omega}\sum_m \beta_m\theta_m = \langle F_m\dot{s}_m\rangle\frac{M}{\Delta\omega} = P^{IN} \tag{112}$$

The accurate expression of the radiative term is [c.f., Eqs. (9.12), (9.13), (9.9a), (9.9b) of Lyon-Maidanik[11]

$$P_{rad} \equiv M \sum_{m}^{N_s} \sum_{r}^{N_r} g_{mr}(\theta'_m - \theta'_r) \tag{113a}$$

$$= M \sum_{m}^{N_s} \sum_{r}^{N_r} g_{mr} \frac{\langle F_m \dot{s}_m \rangle}{\beta_m} - M \sum_{m}^{N_s} \sum_{r}^{N_r} \sum_{r' \neq r}^{N_r} g_{mr} B_{r'm} \langle \dot{q}_{r'} \dot{s}_m \rangle / \beta_m$$

$$- M \sum_{m}^{N_s} \sum_{r}^{N_r} \sum_{m' \neq m}^{N_s} g_{mr} B_{m'r} \langle \dot{s}_{m'} \dot{q}_r \rangle \tag{113b}$$

It is noted that the radiative coefficient as given by Eq. (9.31) of Lyon-Maidanik[11] is

$$R_{rad} = \frac{M}{N_s(\omega)} \sum_{m}^{N_s(\omega)} \sum_{r}^{N_r(\omega)} g_{mr}(\omega_r, \omega_m) \tag{114a}$$

$$\cong \frac{M}{N_s} \sum_{m}^{N_s} \frac{\pi}{2} \overline{B_{mn}^2}^{N_r(\omega)} n_r(\omega) \; ; \quad n_r(\omega) \equiv n_3(\omega) \tag{114b}$$

$$\cong M \frac{\pi}{2} \overline{B_{mn}^2}^{N_r(\omega) \,\&\, m} n_r(\omega) \tag{114c}$$

$$\cong \frac{\rho_0 c_0 k_a^2}{(2\pi \epsilon_s \epsilon_R)} \int_{A_1} \int_{A_2} \frac{1}{2} \overline{\psi_r(\underline{x}_1)\psi_r(\underline{x}_2)}^{N_r(\omega)} \phi_m(\underline{x}_1)\phi_m(\underline{x}_2) \, d\underline{x}_1 \, d\underline{x}_2$$

which checks Eq. (11.1) of the same reference (see Appendix D), if one notes that

$$\overline{\frac{1}{2}\psi_r(\underline{x}_1)\psi_r(\underline{x}_2)}^{N_r} = \overline{[\psi_r(\underline{\tau}_1)\psi_r(\underline{\tau}_2)}^{N_r}]_{\substack{\underline{\tau}_1 \to \underline{x}_1 \\ \underline{\tau}_2 \to \underline{x}_2}} = \frac{1}{8}[\sin(k_a|\underline{x}_1 - \underline{x}_2|)/(k_a|\underline{x}_1 - \underline{x}_2|)] \tag{115}$$

Using this type of approximate processes, it may be possible to reduce Eq. (113b) to a more familiar but improved form. This remains to be a future task of research. Lyon-Maidanik has approximated $\theta'_m - \theta'_r$ by $\langle \dot{s}^2_m \rangle$; however, they have considered only modes of one type. We have changed it to $\langle \dot{s}^2_m \rangle - \langle \dot{q}^2_r \rangle$ in Eq. (35). Both approximations are subject to doubt in a general case.

RECOMMENDATIONS FOR FURTHER RESEARCH

It would appear the general results of this study indicate that use of the statistical energy method is reasonably adequate for prediction of response of coupled cylinder-air systems to excitation by non-reverberant acoustic pressure. Prediction of cylinder response is quite acceptable, while that for the interior air is somewhat less acceptable. It has not been established whether the discrepancies result from the general concepts of the statistical energy method itself, or from erroneous estimates of some coefficient which is used in the method. Thus, considerable additional effort is required before a good overall understanding of the capabilities of the method will be achieved. We will list briefly some of the steps which may be useful to follow in this future effort.

(1) In order to avoid estimating the errors involved in the use of real medium-band filters, it would be better to avoid the use of typical, commercially-available, part-octave filters. As a better approximation, measurements should be made with constant bandwidth, narrow band filters, and the results integrated electronically over the desired part-octave band. A much better approximation of a rectangular filter should result. Unfortunately, this was realized too late in the present program.

(2) Better prediction and measurements of structural damping in cylinders is essential.

(3) The statistical energy method should be applied to studies of various kinds of structural elements. It is surmised that some of its limitations for use on one kind of element may not be so severe on others.

(4) A further review and more general summary of the statistical energy method should be provided. Some recent attempts at this have already been set forth. They are particularly desirable since much of the earlier literature on the method is usually quite terse, and it is fraught with typographical errors and unclear mathematical steps.

(5) As pointed out at the end of the last section, a more complete analysis of the percentage method should be conducted. In particular, the failure of the detailed results for energy density to satisfy the original assumptions, and yet the simultaneous rather good agreement of the overall results should be explained. Other forms of coupling between various modal groups may be developed.

(6) The effect of mesh size on input power coefficients should be determined. In this summary, all integrations were performed with a mesh size of 0.4 in., except for one case. Results for Figures 10 and 11 were also computed for a mesh size of 0.2 in. at a frequency of 3150 only. It was found that some individual joint acceptance integrals changed by as much as 40%, although the net effect was negligible on the total for the band.

(7) In the present experiments, interior air pressures were measured at only a few selected points. Measurement at many points would allow the calculation of a space average which could more directly be compared with predicted results. However, in the presence of wide spatial variations, the practical use of the results is still in question. It would appear that a prediction of maximum response would be of more use than that for the average response.

ACKNOWLEDGMENTS

The authors wish to express their sincere appreciation to several colleagues who aided in the conduct of this work. Special mention should be given to Dr. H. N. Abramson and Dr. U. S. Lindholm for consultation, to Mr. Robert Gonzales for digital computer programming, and to Mr. Mike Sissung for editing the manuscript.

REFERENCES

1. Chandiramani, Khushi L. and Lyon, Richard H., "Response of Structural Components of a Launch Vehicle to In-flight Acoustic and Aerodynamic Environments," The Shock and Vibration Bulletin, 36, Part 5, January 1967, Naval Research Laboratory, Washington, D. C.

2. Barnoski, R. L., Piersol, A. G., Van Der Laan, W. F., White, P. H., and Winter, E. F., "Summary of Random Vibration Prediction Procedures," NASA CR-1302, April 1969.

3. Kana, D. D., "Response of a Cylindrical Shell to Random Acoustic Excitation," Interim Report, Contract No. NAS8-21479, Southwest Research Institute, July 1969. (Also Proceedings of AIAA/ASME 11th Structures, Structural Dynamics, and Materials Conference, Denver, April 22-24, 1970.)

4. White, Pritchard H., "Sound Transmission Through a Finite, Closed, Cylindrical Shell," Jour. Acous. Soc. America, Vol. 40, No. 5, pp. 1124-1130, 1966.

5. Bozich, D. J., and White, R. W., "A Study of the Vibration Responses of Shells and Plates to Fluctuating Pressure Environments," NASA CR 1515, March 1970.

6. Manning, Jerome E. and Maidanik, Gideon, "Radiation Properties of Cylindrical Shells," Jour. of the Acoustical Soc. of Amer., Vol. 36, No. 9, pp. 1691-1698, September 1964.

7. Arnold, R. N. and Warburton, G. B., "The Flexural Vibrations of Thin Cylinders," Jour. Proc. Inst. Mech. Eng. (London), Vol. 167, pp. 62-74, 1953.

8. Ungar, Eric E., "Fundamentals of Statistical Energy Analysis of Vibrating Systems," AFFDL-TR-66-52, May 1966, Wright-Patterson Air Force Base, Ohio.

9. Zeman, J. L. and Bogdanoff, J. L., "A Comment on Complex Structural Response to Random Vibrations," AIAA Journal, Vol. 7, No. 7, pp. 1225-1231, July 1969.

10. Conticelli, V. M., "Study of Vibratory Response of a Payload Subjected to a High Frequency Acoustic Field," Wyle Laboratories Report WR 69-9, May 1969.

11. Lyon, R. H. and Maidanik, G., "Power Flow Between Linearly Coupled Oscillators," Jour. Acous. Soc. of America, Vol. 34, No. 5, pp. 623-639, May 1962.

12. Crocker, M. J. and Price, A. J., "Sound Transmission Using Statistical Energy Analysis," Jour. Sound Vibration, Vol. 9, No. 3, pp. 469-486, 1969.

13. Monse, P. M. and Bolt, R. H., "Sound Waves in Rooms," Reviews of Modern Physics, Vol. 16, No. 2, pp. 64-85, April 1944.

14. Robson, J. D., Random Vibration, Elsevier Publishing Co., New York, 1964.

15. Bendat, J. S. and Piersol, A. G., Measurement and Analysis of Random Data, John Wiley & Sons, Inc., New York, 1966.

16. White, R. H. and Powell, A., "Transmission of Random Sound and Vibration Through a Rectangular Wall," Jour. Acous. Soc. of America, Vol. 40, No. 4, pp. 821-832, 1966.

17. Maidanik, G., "Response of Panels to Reverberant Acoustic Fields," Jour. Acous. Soc. of America, Vol 34, No. 6, pp. 809-826, June 1962.

18. Lyon, R. H., "Noise Reduction of Rectangular Enclosures with One Flexible Wall," Jour. Acous. Soc. of America, Vol. 35, No. 11, pp. 1791-1797, November 1963.

19. Lazan, B. J., Damping of Materials and Members in Structural Mechanics, Pergamon Press, New York, 1968.

20. Baker, W. E., Woolam, W. E., and Young, D., "Air and Internal Damping of Thin Cantilever Beams," Int. Jour. Mech. Sci., Vol. 9, pp. 743-766, Pergamon Press, Ltd., 1967.

21. Boley, B. A. and Weiner, J. H., Theory of Thermal Stress, John Wiley & Sons, Inc., 1960.

22. Beranek, L. L., "Acoustic Properties of Gases," Handbook of Physics, American Institute of Physics, McGraw-Hill, New York, pp. 3-59 to 3-70, 1963.

23. Chu, W. H., "Breathing Vibrations of a Partially Filled Cylindrical Shell - Linear Theory," Jour. Appl. Mech., Vol 30, No. 4, pp. 532-536, December 1963.

24. McLachlan, N. W., Bessel Functions for Engineers, 2nd editor, Oxford University Press, London, 1955.

APPENDIX A

SPATIAL DISTRIBUTION PARAMETERS FOR ACOUSTICAL FIELD

SPK. SPATIAL DISTRIBUTION EMPIRICAL EQUATION CONSTANTS

1/3-Octave Center Frequency	A_0	B_0	P_0	$D_0 \times 10^2$	$E_0 \times 10^2$	G_0
100	3.47×10^{-2}	2.682	150.0	0	0	0
125	3.47×10^{-2}	2.682	150.0	0	0	0
160	3.47×10^{-2}	2.682	150.0	0	0	0
200	3.47×10^{-2}	2.682	150.0	0	0	0
250	3.47×10^{-2}	2.682	150.0	0	0	0
315	3.47×10^{-2}	2.682	150.0	0	0	0
400	3.47×10^{-2}	2.682	150.0	0	0	0
500	3.47×10^{-2}	2.682	150.0	0	0	0
630	3.47×10^{-2}	2.682	150.0	0	0	0
800	3.47×10^{-2}	2.682	150.0	8.0	8.0	6.0
1000	0.00856	2.430	150.0	6.0	6.0	4.0
1250	0.00172	1.906	11.0	15.0	15.0	4.0
1600	0.00520	2.130	9.0	-10.0	-10.0	4.0
2000	0.3752	0.813	3.0	-20.0	-20.0	3.3
2500	0.1685	0.799	4.05	60.0	40.0	2.5
3150	0.0836	2.330	5.25	12.0	4.0	2.5
4000	0.3092	0.724	2.00	30.0	-8.0	1.5

C0

$$k_R = \exp(-A_0 R^{B_0}) \cos\left(\frac{\pi R}{P_0}\right) \quad \text{for } R \leq 8.0\dagger$$

Quad

$$k_I = D_0 \cos\left(\frac{\pi R}{G_0}\right) - E_0 \quad \text{for } R \leq 8.0\ddagger$$

†For f = 2500 $k_x = 1.00$ for $R \leq 1.5$

‡For f = 4000 $k_y = 0.00$ for $R \leq 1.0$

APPENDIX B

SPEAKER CALIBRATION FACTORS

SPEAKER CALIBRATION CONSTANTS

1/3-O Center Freq.	1/3-O Band into Spk. No. Eq. $(psi/V_{cms})^2 \times 10^6$	1/3-O Center Freq.	1/3-O Band into Spk. No. Eq. $(psi/V_{cms})^2 \times 10^6$
100	0.989	630	3.04
125	1.113	800	3.98
160	1.043	1000	5.66
200	0.937	1250	1.855
250	0.967	1600	1.633
315	1.026	2000	1.056
400	1.336	2500	0.432
500	2.02	3150	0.244
		4000	0.311
		5000	0.476

APPENDIX C

DERIVATION OF EQ. (49)

DERIVATION OF EQ. (49)

For narrow-band sampling, consider

$$p_1 = p_1^R \cos(\omega t) + p_1^I \sin(\omega t) \tag{C-1}$$

$$p_2 = p_2^R \cos(\omega t) + p_2^I \sin(\omega t) \tag{C-2}$$

Define p° as p with 90° shift[15]. We have

$$p_j^\circ = - p_j^R \sin(\omega t) + p_j^I \cos(\omega t), \quad j = 1, 2 \tag{C-3}$$

The time averages yield

$$\hat{Q}_{p_1 p_2} = \langle p_1 p_2^\circ \rangle = \frac{1}{2}(p_1^R p_2^I - p_1^I p_2^R) = - \langle p_2 p_1^\circ \rangle = Q_{p_2 p_1} \tag{C-4}$$

$$\hat{C}_{p_1 p_2} = \langle p_1 p_2 \rangle = \frac{1}{2}(p_1^R p_2^R + p_1^I p_2^I) = \langle p_2 p_1 \rangle = C_{p_2 p_1} \tag{C-5}$$

Let

$$p = p(\underline{x}, t), \quad p' = p(\underline{x}', t), \quad p'' = p(\underline{x}'', t), \quad p_0 = p(0, t) \tag{C-6a, b, c}$$

By approximating the measured data, we have

$$\hat{C}_{p_0 p} = k_R(\underline{x}, \omega) S_{p_0}(\omega), \quad \hat{Q}_{p_0 p} = k_I(\underline{x}, \omega) S_{p_0}(\omega) \tag{C-7a, b}$$

where

$$S_{p_0}(\omega) = \hat{C}_{p_0 p_0} = G_{p_0 p_0} = \frac{1}{2}[(p_0^R)^2 + (p_0^I)^2] \tag{C-8}$$

For convenience, define $p^R = p_R$; then, we have

$$\hat{Q}_{p'p_0} = \frac{1}{2}(p'_R p^I_0 - p'_I p^R_0) = - k_I(\underline{x}', \omega) S_{p_0}(\omega) \qquad \text{(C-9)}$$

$$\hat{Q}_{p''p_0} = \frac{1}{2}(p''_R p^I_0 - p''_I p^R_0) = - k_I(\underline{x}'', \omega) S_{p_0}(\omega) \qquad \text{(C-10)}$$

Multiplication of Eqs. (C-8) and (C-9) gives

$$k_I(\underline{x}', \omega) k_I(\underline{x}''\omega) S^2_{p_0}(\omega) = \frac{1}{4}[p'_R p''_R (p^I_0)^2 + p'_I p''_I (p^R_0)^2 - (p'_I p''_R + p''_R p''_I) p^R_0 p^I_0] \qquad \text{(C-11)}$$

Similarly, one obtains

$$k_R(x', \omega) k_R(\underline{x}'', \omega) S^2_{p_0}(\omega) = \frac{1}{4}[p'_R p''_R (p^R_0)^2 + p'_I p'_I (p^I_0)^2 + (p'_I p''_R + p'_R p''_I) p^R_0 p^I_0] \qquad \text{(C-12)}$$

Adding of Eqs. (C-11) and (C-12) yields

$$\frac{1}{4}[p'_R p''_R + p'_I p''_I][(p^R_0) + (p^I_0)^2] = [k_I(\underline{x}', \omega) k_I(\underline{x}'', \omega) + k_R(\underline{x}', \omega) k_R(\underline{x}'', \omega)] S^2_{p_0}(\omega) \qquad \text{(C-13)}$$

Dividing Eq. (C-13) by S_{p_0} with Eqs. (C-8) and (C-5), one finds

$$\hat{C}_{p'p''} = [k_I(\underline{x}, \omega) k_I(\underline{x}', \omega) + k_R(\underline{x}, \omega) k_R(\underline{x}'', \omega)] S_{p_0}(\omega), \quad \text{(Q.E.D)} \qquad \text{(C-14)}$$

APPENDIX D

DERIVATION OF EQS. (114b) AND (105)

DERIVATION OF EQS. (114b) AND (105)

We have Eq. (9.11) of Lyon-Maidanik[11] that

$$g_{mr} = \frac{B_{mr}^2(\beta_m\omega_r^2 + \beta_r\omega_m^2)}{(\omega_m^2 - \omega_r^2)^2 + (\beta_m + \beta_r)(\beta_m\omega_r^2 + \beta_r\omega_m^2)} \tag{D-1}$$

By changing summation to integration by assuming there is a large number of air modes as done by Lyon-Maidanik and by residue theorem after taking advantage of the δ-function type integrand, we found that

$$\begin{aligned}
\sum_r^{N_r} g_{mr} &= \overline{B_{mr}^2}^{N_r(\omega)} \int_{\omega - \Delta\omega/2}^{\omega + \Delta\omega/2} \frac{(\beta_m\omega_r^2 + \beta_r\omega_m^2)\, n_r(\omega_r)\, d\omega_r}{(\omega_m^2 - \omega_r^2)^2 + (\beta_r + \beta_m)(\beta_m\omega_r^2 + \beta_r\omega_m^2)} \\
&\cong \overline{B_{mr}^2}^{N_r(\omega)}\, n_r(\omega) \int_0^{\infty} \frac{(\beta_m\omega_r^2 + \beta_r\omega_m^2)\, d\omega_r}{(\omega_m^2 - \omega_r^2)^2 + (\beta_r + \beta_m)(\beta_m\omega_r^2 + \beta_r\omega_m^2)} \\
&= \frac{1}{2}\overline{B_{mr}^2}^{N_r(\omega)}\, n_r(\omega) \int_{-\infty}^{\infty} \frac{(\beta_m\omega_r^2 + \beta_r\omega_m^2)\, d\omega_r}{(\omega_r^2 - \omega_m^2) + (\beta_r + \beta_m)(\beta_m\omega_r^2 + \beta_r\omega_m^2)} \\
&= \frac{\pi}{2}\overline{B_{mr}^2}^{N_r(\omega)}\, n_r(\omega)
\end{aligned} \tag{D-2}$$

which justifies Eq. (114b) from Eq. (114a). Next, we shall derive Eq. (105).

From Eq. (9.6) of Lyon-Maidanik

$$B_{mr} = B_{rm} = \left(\frac{\rho_0 c_0^2}{MV\epsilon_r\epsilon_m}\right)^{1/2} \int_A \psi_r(\underset{\sim}{x})\, \phi_m(\underset{\sim}{x})\, d\underset{\sim}{x} \tag{D-3}$$

Then

$$\overline{B_{mn}^2 N_r(\omega)} = \left(\frac{\rho_0 c_0^2}{MV\epsilon_r\epsilon_m}\right)^{1/2} \int_{A_1}\int_{A_2} \overline{\psi_r(\underline{x}_1)\psi(\underline{x}_2)\, N_r(\omega)}\, \phi_m(\underline{x}_1)\phi_m(\underline{x}_2)\, d\underline{x}_1\, d\underline{x}_2 \tag{D-4}$$

Since $\psi_r(\underline{x})$ is a two-dimensional vector function on the shell surface, we only have two components of the surface vector; therefore, in place of Eq. (7.13) of Lyon-Maidanik, we should use

$$\psi_r(\underline{x}_1)\psi_r(\underline{x}_2) = \frac{1}{16} \prod_{h=1}^{2} \prod_{j=1}^{2} \left[e^{ik_j x_{hj}} + e^{-ik_j x_{hj}}\right] \tag{D-5}$$

Now, instead of 8 positions in space, we only have 4 positions on the surface that the exponent has minimum value proportional to the difference of x_1 and x_2 such as $\exp[k_x(x_{11} - x_{21}) + k_y(x_{12} - x_{22})]$. Now, we should average with respect to k_x and k_y over the circle of radius $k_a' = (k_x^2 + k_y^2)^{1/2} = (k_a^2 - k_z^2)^{1/2}$ and average over k_z from zero to k_a. Therefore, with θ as the angle between the vector $\underline{k}_a'$ and $\underline{x}_1 - \underline{x}_2$, we have

$$\overline{\psi_r(\underline{x}_1)\psi_r(\underline{x}_2)\, N_r(\omega)} \cong \frac{1}{4} \cdot \frac{1}{2\pi k_a} \int_0^{k_a}\int_0^{2\pi} e^{i\left[|\underline{x}_1 - \underline{x}_2| \sqrt{k_a^2 - k_z^2}\cos\theta\right]} d\theta\, dkz \tag{D-6}$$

$$= \frac{1}{4k_a} \int_0^{k_a} J_0\left(|\underline{x}_1 - \underline{x}_2| \sqrt{k_a^2 - k_z^2}\right) dkz \tag{D-7}$$

$$= \frac{1}{4k_a} \left[\frac{\sin\left(|\underline{x}_1 - \underline{x}_2|\, kz\right)}{|\underline{x}_1 - \underline{x}_2|}\right]_0^{k_a} = \frac{1}{4} \frac{\sin\left(k_a|\underline{x}_1 - \underline{x}_2|\right)}{k_a|\underline{x}_1 - \underline{x}_2|} \tag{D-8}$$

Equations (D-7) and (D-8) were derived with well-known formulas given by McLachlan (2nd edition)[24]. If we follow through the factors in Lyon-Maidanik's paper, we can show that

$$\left[\frac{\qquad\qquad N_r(\omega)}{\psi_r(\underline{\tau}_1)\psi_r(\underline{\tau}_2)}\right]_{\substack{\tau_1 \to x_1 \\ \tau_2 \to x_2}} = \frac{1}{8}\,\frac{\sin\left(k|\underline{x}_1 - \underline{x}_2|\right)}{k|\underline{x}_1 - \underline{x}_2|} = \Psi(\underline{x}_1, \underline{x}_2)_{\text{Lyon-Maidanik}} \tag{D-9}$$

as there were 8 positions in space divided by 64. The factor $\frac{1}{8}$ should be present in Eq. (7.16) of Lyon-Maidanik and Eq. (2.18) of Maidanik.

Equations (D-8) and (D-9) verify Eq. (115). The final result of Lyon-Maidanik was correct as they had a factor 2 too large in using their Eq. (9.17) instead of Eq. (D-2) and a factor 2 too small by using Eq. (D-9) instead of the correct average Eq. (D-8). It may be stated that Eq. (114c) yields Eqs. (2.15) and (2.21) of Maidanik, which rightfully yields the approximate radiation formulas, Eqs. (2.24), (2.25) in his paper with his approximation Eq. (A-1); namely,

$$\begin{aligned} R_{rad} &\cong A\rho_0 c_0\left[1 - (k_x/k_a)^2\right]^{-1/2} \cong A\rho_0 c_0\left[1 - (k_y/k_a)^2\right]^{-1/2} \\ &\cong A\rho_0 c_0\left[1 - (k_p/k_a)^2\right]^{-1/2} \text{ for } k_p < k_a, \text{ AF modes} \end{aligned} \tag{D-10}$$

$$R_{rad} \cong 2(A\rho_0 c_0/3\pi^{1/2})(\ell k_p^2/k_x)^{1/2}$$

$$\cong 2(A\rho_0 c_0/3\pi^{1/2})(hk_p^2/k_y)^{1/2} \tag{D-11}$$

$$\cong (A\rho_0 c_0/3\pi^{1/2})\left[(\ell k_p^2/k_x)^{1/2} + (hk_p^2/k_y)^{1/2}\right] \quad k_p \cong k_a$$

Due to time limitation, however, Eqs. (2.39a, b, c) of Maidanik have not been rederived. However, at least Eq. (2.39a) was checked and corrected by Crocker-Price and is used for AS modes ($k_p > k_a$) in this paper.